A&A 639, A133 (2020)
https://doi.org/10.1051/0004-6361/202037438

Astronomy & Astrophysics

Distance, magnetic field, and kinematics of the filamentary cloud LDN 1157

Ekta Sharma[1,2], Maheswar Gopinathan[1], Archana Soam[3,4], Chang Won Lee[4,5], Shinyoung Kim[4], Tuhin Ghosh[6], Anandmayee Tej[7], Gwanjeong Kim[9], Neha Sharma[8], and Piyali Saha[1]

[1] Indian Institute of Astrophysics, Koramangala, Bangalore 560034, India
e-mail: ekta.sharma@iiap.res.in
[2] Department of Physics and Astrophysics, University of Delhi, Delhi 110007, India
[3] SOFIA Science Centre, USRA, NASA Ames Research Centre, MS-12, N232, Moffett Field, CA 94035, USA
[4] Korea Astronomy & Space Science Institute, 776 Daedeokdae-ro, Yuseong-gu, Daejeon, Republic of Korea
[5] University of Science and Technology, Korea, 217 Gajeong-ro, Yuseong-gu, Daejeon 34113, Republic of Korea
[6] School of Physical Sciences, National Institute of Science Education and Research, HBNI, Jatni 752050, Odisha, India
[7] Indian Institute of Space Science and Technology, Valiamala PO, Thiruvananthapuram - 695547 Kerala, India
[8] School of Space Research, Kyung-Hee University, 1732, Deogyeong-daero, Giheung-gu, Yongin-si, Gyeonggi-do 17104, Republic of Korea
[9] Nobeyama Radio Observatory, National Astronomical Observatory of Japan, National Institutes of Natural Sciences, Nobeyama, Minamimaki, Minamisaku, Nagano 384-1305, Japan

Received 2 January 2020 / Accepted 27 March 2020

ABSTRACT

Context. LDN 1157 is one of several clouds that are situated in the cloud complex LDN 1147/1158. The cloud presents a coma-shaped morphology with a well-collimated bipolar outflow emanating from a Class 0 protostar, LDN 1157-mm, that resides deep inside the cloud.
Aims. The main goals of this work are (a) mapping the intercloud magnetic field (ICMF) geometry of the region surrounding LDN 1157 to investigate its relationship with the cloud morphology, outflow direction, and core magnetic field (CMF) geometry inferred from the millimeter- and submillimeter polarization results from the literature, and (b) to investigate the kinematic structure of the cloud.
Methods. We carried out optical (*R*-band) polarization observations of the stars projected on the cloud to map the parsec-scale magnetic field geometry. We made spectroscopic observations of the entire cloud in the ^{12}CO, C^{18}O, and N_2H^+ ($J = 1$–0) lines to investigate its kinematic structure.
Results. We obtained a distance of 340 ± 3 pc to the LDN 1147/1158, complex based on the *Gaia* DR2 parallaxes and proper motion values of the three young stellar objects (YSOs) associated with the complex. A single filament of ∼1.2 pc in length (traced by the *Filfinder* algorithm) and ∼0.09 pc in width (estimated using the *Radfil* algorithm) is found to run throughout the coma-shaped cloud. Based on the relationships between the ICMF, CMF, filament orientations, outflow direction, and the hourglass morphology of the magnetic field, it is likely that the magnetic field played an important role in the star formation process in LDN 1157. LDN 1157-mm is embedded in one of the two high-density peaks detected using the *Clumpfind* algorithm. The two detected clumps lie on the filament and show a blue-red asymmetry in the ^{12}CO line. The C^{18}O emission is well correlated with the filament and presents a coherent structure in velocity space. Combining the proper motions of the YSOs and the radial velocity of LDN 1147/1158 and an another complex, LDN 1172/1174, that is situated ∼2° east of it, we found that the two complexes are moving collectively toward the Galactic plane. The filamentary morphology of the east-west segment of LDN 1157 may have formed as a result of mass lost by ablation through interaction of the moving cloud with the ambient interstellar medium.

Key words. ISM: clouds – polarization – ISM: magnetic fields – ISM: individual objects: L1157 – dust, extinction – ISM: kinematics and dynamics

1. Introduction

Observations from the *Herschel* Space Observatory, with its unprecedented sensitivity and resolution, revealed the omnipresence of a deep network of filaments (André et al. 2010; Men'shchikov et al. 2010) in quiescent and star-forming molecular clouds (e.g., Myers 2009; André et al. 2010; Arzoumanian et al. 2011; Kirk et al. 2013; Rivera-Ingraham et al. 2016). These filaments are often found to extend from dense star-forming hubs (Myers 2009; Liu et al. 2012; Galván-Madrid et al. 2013), and more star-forming sites are distributed along their length (e.g., Myers 2009; Schneider et al. 2012; André et al. 2014; Tafalla & Hacar 2015). These filamentary structures are described as either stagnant gas produced by large-scale compression flows (Peretto et al. 2012) or isothermal self-gravitating cylinders in pressure equilibrium with external medium (Fischera & Martin 2012; Heitsch 2013), or they are supported by helical magnetic fields (Fiege & Pudritz 2000a). To gain more insight into the processes involved in the formation of these filaments, it is important to study their internal structure, magnetic field geometry, and kinematics of gas.

Several models and simulations have been carried out to understand processes such as iso-thermal-driven turbulence (Padoan & Nordlund 2002; de Avillez & Breitschwerdt 2005;

Moeckel & Burkert 2015), thermal (Vázquez-Semadeni et al. 2003; Audit & Hennebelle 2005; Heitsch et al. 2008) or gravitational (Nakajima & Hanawa 1996; Umekawa et al. 1999; Van Loo et al. 2014) instabilities that might influence the formation of filamentary structures in molecular clouds. Filaments in unbound and non-star-forming regions (Miville-Deschênes et al. 2010) suggest a paradigm in which they represent the early stages of core and star formation. In this paradigm, the dense material within molecular clouds is first accumulated into dense filaments that then fragment to form star-forming cores (Balsara et al. 2001; Gómez & Vázquez-Semadeni 2014). These fragments may continue to amass material through gravitational inflow, resulting in a flow pattern parallel to the filament axis (e.g., Balsara et al. 2001; Banerjee et al. 2006). Correlated magnetic fields on scales of 1–10 pc have been observed in interstellar clouds (e.g., Vrba et al. 1976; Heyer et al. 1987; McCutcheon et al. 1986; Goodman et al. 1992; Pereyra & Magalhães 2004; Chapman et al. 2011; Soam et al. 2015, 2017; Wang et al. 2017; Clemens et al. 2018). The magnetic fields may play an important role in regulating these flows. It is still unclear exactly how the magnetic fields, turbulence, and self-gravity compete or collaborate to form filaments first, then cores, and finally, stars.

According to Gómez & Vázquez-Semadeni (2014) and Smith et al. (2016), filaments arise as a result of anisotropic global collapse of the clouds. Initially, gas is accreted onto the cloud from the surrounding environment, and the magnetic field is expected to be perpendicular to the filament axis. While the low-density material is found to be aligned with the field lines, the dense filaments are seen perpendicular to the magnetic fields (Planck Collaboration Int. XXXII 2016; Planck Collaboration Int. XXXV 2016). This trend is also seen in the polarization observations of background stars in optical (e.g., Heiles 2000; Pereyra & Magalhães 2004; Alves et al. 2008) and near-infrared wavelengths (e.g., Goodman et al. 1992; Chapman et al. 2011). However, as the gas density increases, the gas tends to flow along the filaments, dragging the field lines along with it and causing them to lie parallel to the filament axis (Gómez et al. 2018). The relative orientation of filaments with respect to the local magnetic fields (e.g., Li et al. 2009) and the kinematics of the gas both perpendicular and parallel to the filaments are therefore some observational signatures that are important for understanding the manner in which the material was accumulated during filament formation. To do this, it is crucial to identify and characterize isolated filaments that are at their earliest evolutionary stage of star formation.

In this paper, we present results of a study conducted on an isolated star forming molecular cloud LDN 1157 (L1157). The cloud is located in the Cepheus flare region and is spatially (Lynds 1962; Dutra & Bica 2002) and kinematically (Yonekura et al. 1997) associated with a complex containing a number of clouds: LDN 1147/1148/1152/1155/1157/1158 (hereafter L1147/1158 complex). There is an ambiguity in the adopted distance of the cloud. The most widely quoted distance of L1147/1158 is 325 ± 13 pc (Straizys et al. 1992). However, in several studies, distances of 250 pc (e.g., Looney et al. 2007; Podio et al. 2016) and 440 pc (e.g., Gueth et al. 1996; Avery & Chiao 1996) are also used. L1157 harbors a cold, extremely red object, IRAS 20386+6751 (hereafter L1157-mm), classified as a Class 0 source (Andre et al. 1993; Andre 1996) having a bolometric luminosity of 11 $L_{\odot}$ and bolometric temperature between 60–70 K (Gueth et al. 1997). The source shows a well-collimated bipolar outflow of ∼5′ spatial size (Bachiller et al. 2001) and a ∼2′ flattened envelope perpendicular to it (Looney et al. 2007). The position angle of the outflow measured counterclockwise from the north is 161° (Bachiller et al. 2001) with an inclination angle of ∼10° (Gueth et al. 1996). The magnetic field orientation inferred from 1.3 mm polarization measurements shows an hourglass morphology, with the central vectors showing a position angle of ∼148° measured counterclockwise from north (Stephens et al. 2013).

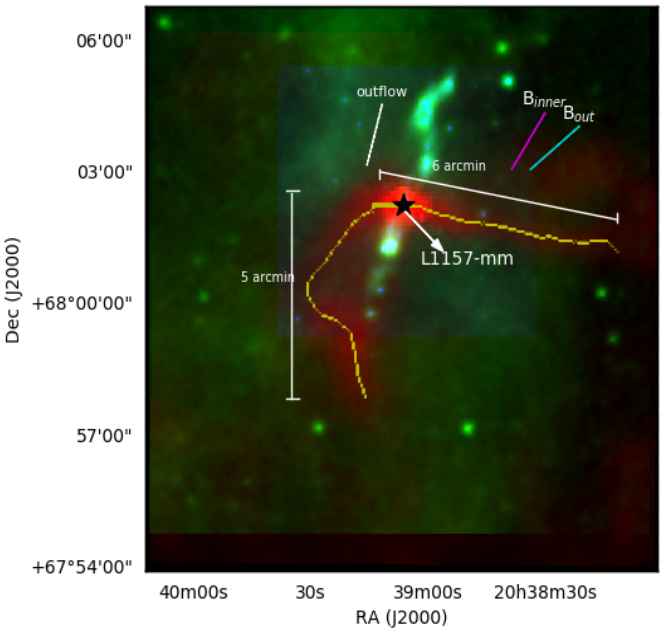

Fig. 1. Color-composite image of the filamentary cloud L1157 made using *Herschel* 250 μm (red), WISE 12 μm (green), and *Spitzer* 8 μm emission (blue). A filament structure in yellow based on the dust column density ($N(H_2)$) distribution extracted using the *Filfinder* algorithm is also shown. The white segment shows the orientation of the outflow, and magenta and cyan segments represent the orientation of inner (traced for submm polarization emission measurements) and outer magnetic fields (traced for the optical polarization measurements of background stars), respectively.

Using the column density map produced from the *Herschel* images, we traced a single filament that runs almost in the east-west direction and then changes its direction toward the south. The filament was traced using the *Filfinder* algorithm (described in Sect. 3.2). Both the east-west and the north-south segments of the filament are found to be ∼5′ in length. In Fig. 1 we show a color-composite image of the region containing the cloud L1157. The image was produced using the *Herschel* 250 μm, WISE 12 μm, and *Spitzer* 8 μm emission. Emission from the protostar, the bipolar outflow originating from it, and a well-defined filament structure extending to the west of the protostar is conspicuous in Fig. 1. The age estimates of L1157-mm, ∼150 kyr (Bachiller et al. 2001; Froebrich 2005; Arce et al. 2008), suggest that the star formation was only recently initiated in L1157, and the conditions that led this cloud to form star(s) may therefore still be preserved. Additionally, the absence of any active high-mass star formation in the vicinity of L1157 (Kun et al. 2009) presents a simple case of isolated low-mass star formation occurring in a quiescent environment.

In this work, we first estimate the distance to L1147/1158 complex using the recently released *Gaia* DR2 parallax and proper motion values of the young stellar object (YSO) candidates associated with it. To investigate the role played by the parsec-scale magnetic field in the formation of L1157, we made optical *R*-band polarization measurements of stars that are

projected on a region of $20' \times 20'$ field that includes the cloud. Because the *Herschel* continuum dust maps lack kinematic information, we made molecular line observations of the region containing the filament structure in L1157 in the ^{12}CO, C^{18}O, and N_2H^+ ($J = 1-0$) lines. Finally, using the *Gaia* DR2 proper motion values of the YSOs associated with the L1147/1158 and L1172/1174 complexes (an another complex situated 2° east of L1147/1158) and using the radial velocities of the cloud, we determine the motion of the complexes in space and discuss a possible origin of the filament in L1157.

The paper is organized in the following manner. We begin with a brief description of the observations, data, and the reduction procedure in Sect. 2. The results from the polarization and molecular line observations are presented in Sect. 3. We discuss the results we obtained in Sect. 4. We conclude the paper with a summary of the results in Sect. 5.

2. Observations and data reduction

2.1. Optical polarimetry

The polarimetric observations presented here were carried out over several nights in November 2015 at the Cassegrain focus of the 104 cm Sampurnanand Telescope, Nainital, India. We used the Aries IMaging POLarimeter (AIMPOL), which incorporates an achromatic rotatable half-wave plate (HWP) as modulator and a Wollaston prism beam splitter as the analyzer. The fast axis of the HWP and the axis of the Wollaston prism are kept perpendicular to the optical axis of the system. The fast axis of the HWP is rotated at four different angles 0°, 22.5°, 45°, and 67.5°. This provides two images of the object on the field of CCD camera that is of TK 1024×1024 pixel^2 size (see Rautela et al. 2004). The plate scale and the gain of the CCD used are 1.48″ per pixel and 11.98 e$^-$ per ADU (analog-to-digital unit). The noise created while the CCD is read out is 7.0 e^{-1}.

A standard Johnson R_{kc} filter with λ_{eff} as 0.76 μm was used for polarimetric observations. The spatial resolution (full width at half-maximum, FWHM) corresponds to 2–3 pixels on the CCD. The data reductions are carried out using a software developed in Python to identify the ordinary and corresponding extraordinary images of each object in the field of view. The photometry is carried out using aperture photometry provided by the Image Reduction and Analysis Facility (IRAF) package. The intensities of ordinary and extraordinary images in the observed field are extracted to calculate the required ratio $R(\alpha)$. This ratio is defined as

$$R(\alpha) = \frac{\frac{I_e(\alpha)}{I_o(\alpha)} - 1}{\frac{I_e(\alpha)}{I_o(\alpha)} + 1} = P\cos(2\theta - 4\alpha), \quad (1)$$

where P is the strength of the total linearly polarized light, θ is the polarization angle in the plane of sky, and α is the angle of the half-wave plate fast axis with respect to the axis of the Wollaston prism. P and θ are calculated using normalized Stokes parameters q1, u1, and q2, u2 at angles 0°, 22.5°, 45°, and 67.5° respectively.

Standard polarized and unpolarized stars selected from Schmidt et al. (1992) are observed routinely to correct the polarization position angle offset and the instrumental polarization, respectively. The instrumental polarization derived from the unpolarized standards is found to be ∼0.1% (e.g., Medhi et al. 2008; Soam et al. 2013). The polarization angles of the standard stars obtained from our observations were compared with those of the standard star values given by Schmidt et al. (1992), and the difference was applied as a correction to the polarization angles. In Table 1 we show the log of the polarization observations.

Table 1. Polarized standard stars observed in R_{kc} band.

Date of observation	$P \pm \epsilon_P$ (%)	$\theta \pm \epsilon_\theta$ (°)
HD 236633 (Standard values: 5.38 ± 0.02%, 93.04 ± 0.15°) [a]		
3 November 2015	4.9 ± 0.1	99 ± 1
15 November 2015	5.0 ± 0.1	101 ± 1
16 November 2015	5.1 ± 0.1	101 ± 1
17 November 2015	4.9 ± 0.1	101 ± 1
BD+59°389 (Standard values: 6.43 ± 0.02%, 98.14 ± 0.10) [a]		
2 November 2015	6.3 ± 0.1	105 ± 1
3 November 2015	6.2 ± 0.1	105 ± 1
15 November 2015	6.0 ± 0.1	106 ± 1
16 November 2015	5.9 ± 0.1	105 ± 1
17 November 2015	6.2 ± 0.1	106 ± 1

References. [a]Values in the R band taken from Schmidt et al. (1992).

2.2. Radio observations

The molecular chemistry is different at various layers of the molecular cloud, which makes it difficult to discuss the kinematics with a single molecular tracer. We have chosen a set of molecules ^{12}CO ($J = 1-0$), C^{18}O ($J = 1-0$), and N_2H^+ ($J = 1-0$) to be observed with the same telescope to constitute a homogeneous set of same calibration. Because of the high difference in dipole moment of N_2H^+ and ^{12}CO molecules, these data are sensitive to high- as well as low-density regions by using these tracers. The filamentary structure of L1157 cloud was mapped with these tracers using the 13.7 m diameter single-dish radio facility at Taeudek Radio Astronomy Observatory (TRAO), which is located at the Korea Astronomy and Space Science Institute (KASI) in Daejeon, South Korea. It operates in the wavelength range of 85–115 GHz. Observations were taken using the new receiver system Second QUabbin Observatory Imaging Array-TRAO (SEQUOIA-TRAO). It consists of high-performing 16 pixel MMIC preamplifiers in a 4×4 array. The pointing accuracy was achieved to be $\leq 5''$ using a standard X Cygnus source in the SiO line. The position-switch mode was employed to subtract the sky signals. At 115 GHz, the beam size (half-power beam width, HPBW) of the telescope is about 45″ and the fraction of the beam pattern subtending main beam (beam efficiency) is 51 ± 2%. The system temperature was 550 K-600 K during the observations. The back-end system with fast Fourier transform spectrometer has 4096×2 channels at 15 kHz resolution (∼0.05 km s^{-1} at 110 GHz). Because the optical system provides two side-bands, two different lines can be observed simultaneously. The C^{18}O line, which reveals the dynamics of high-density regions of the cloud, was simultaneously observed with ^{12}CO. The observations were performed using the on-the-fly (OTF) mapping technique, covering a region of $12' \times 12'$ for ^{12}CO and C^{18}O and a $8' \times 8'$ region for N_2H^+ in $J = 1-0$ transition. The center of the maps was 20h39m06.19s +68°02′15.09″. The signal-to-noise ratio (S/N) for the ^{12}CO line at the position 20h39m12.837s +68°01′06″ is found to be ∼18 with the peak T_A^* as 3.87 K and rms as 0.22 K at a velocity resolution of 0.06 km s^{-1} . The spectra were reduced using the CLASS software of the IRAM GILDAS software package.

A first-order polynomial was applied to correct the baseline in the final spectra. The resulting 1σ rms noise levels in $T_A{}^*$ scale are ~0.3 K for ^{12}CO (1–0) and 0.1 K for the C^{18}O line, respectively. The final data cubes have a cell size of 22″ and a 0.06 km s^{-1} velocity channel width.

3. Results

3.1. Polarization results

We made optical polarization measurements of 62 stars that are projected on an area of $0.3^\circ \times 0.3^\circ$ around the protostar L1157-mm. We show the measured degree of polarization (P%) and polarization position angles (θ_P) in Fig. 2. The polarization measurements for which the ratio of P% and its corresponding error is greater than 3 are plotted. For the majority of the sources, P% ranges between ~1−2% and the θ_P ranges between ~110°−140°. The mean values of P% and θ_P of the sources showing P% $\geqslant 1$ are 2.1 and 129°, respectively and the corresponding standard deviation values are 0.6 and 11°, respectively. We also show the polarization values of 16 sources selected from a circular area of 5° radius about the protostar. Although 18 sources are present within our search radius, we rejected 2 sources: HD 200775 and HD 193533. The first, HD 200775, is an intermediate-mass Herbig Be star causing a reflection nebulosity, NGC 7023. Source HD 200775 is situated at a distance of 357 ± 6 pc (Bailer-Jones et al. 2018) and the P% and θ_P values given in the Heiles (2000) catalog are ~0.8 ± 0.2 and ~92° ± 7°. It is highly likely that the polarization measurements are affected by the intense emission from the nebulosity surrounding the star due to scattering. The second star, HD 193533, is an M3III and is classified as a variable star in the Simbad database. The distance, P%, and θ_P values for this star are 301 ± 5 pc, 0.3 ± 0.05, and 142° ± 4°, respectively.

3.2. Identification of filaments and clumps

The whole L1147/1158 complex was observed by the *Herschel* telescope. The PACS (Poglitsch et al. 2010) and SPIRE (Griffin et al. 2010) instruments were used to observe the region simultaneously at 70, 160, 250, 350, and 500 μm wavelengths as a part of the Gould Belt Survey (André et al. 2010). The 160–500 μm *Herschel* images were used to construct an H_2 column density map and a dust temperature map of the entire complex at the spatial resolution of 36″. The units of the SPIRE images, which are in MJysr^{-1}, were changed into Jy pixel^{-1} using the task *convertImageunit* in the *Herschel* Interactive Processing Environment (HIPE). To fit the spectral energy distribution (SED) on a pixel-to-pixel basis, all the maps (PACS 160, and SPIRE 250 μm, 350, and 500 μm) were convolved to the 500 μm image using the kernels from Aniano et al. (2011) and regridded to a pixel scale of 14″. The background flux density (I_{bg}) was determined using values from the pixels in a relatively darker patch in the sky. The emission of every pixel is assumed to be represented by a modified blackbody emission,

$$S_\nu(\nu) = \Omega(1 - \exp(-\tau_\nu))B_\nu(\nu, T_d), \quad (2)$$

with

$$\tau_\nu = 0.1 \mu m_H \kappa_\nu N_{H_2}, \quad (3)$$

where $S_\nu(\nu)$ is the observed flux density for a given frequency ν and the solid angle Ω, $\tau(\nu)$ is the optical depth, $B(\nu,T_d)$ is the Planck function, T_d is the dust temperature, m_H is the mass

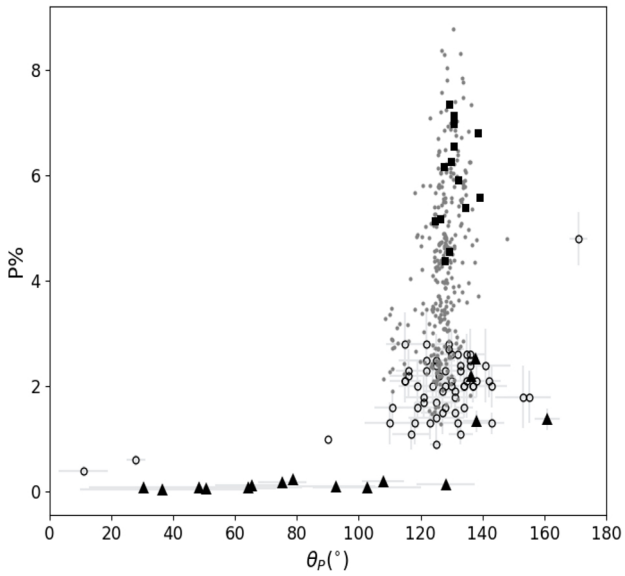

Fig. 2. P% vs. θ_P for the 62 sources (open circles) projected over an area of $0.3^\circ \times 0.3^\circ$ around the protostar L1157-mm. The measurements are made in R_{kc} filter. The *Planck* polarization results (see Sect. 4.2) from within a 1° region around cloud L1157 are shown using filled gray circles. The *Planck* results from the region in which we carried out the optical polarization observations are shown using black squares. We also show the polarization values (filled triangles) of the sources distributed in a circular region of 5° radius about the protostar obtained from the Heiles (2000) catalog.

of hydrogen, μ_{m_H} is the mean molecular weight taken as 2.8 (Kauffmann et al. 2008), and N_{H_2} is the column density for hydrogen. All the fluxes were normalized to Jy pixel^{-1}. For the opacity, we assumed a functional form of $\kappa_\nu = 0.1\ (\frac{\nu}{1000\,\mathrm{GHz}})^\beta$, where β is the spectral emissivity index, and the value was taken as 2 (Schnee et al. 2010). The derived column density and dust temperature maps were regridded using the Astronomical Image Processing System (AIPS) to 3″. Because we modeled the cold dust emission longward of 160 μm, the fit was relatively poorer near the protostar where contribution from warm dust would also be present. This prevented us from using a single blackbody model.

To characterize the filament properties, we used the *FilFinder* algorithm to extract the filaments from the column density map. The *FilFinder* algorithm was developed to extract filamentary structures in clouds observed by *Herschel* (André et al. 2010). The extraction was performed by reducing the regions of interest to topological skeletons based on specified threshold intensities. Each element of the skeletons therefore represents the medial position within the extents of the required region (Koch & Rosolowsky 2015). The emission structures in L1157 were flattened to a percentile of 99 to smoothen the bright features in the image. While creating masks, the global threshold was taken as ~2.1×10^{21} cm^{-2} (3σ above the background, $\sigma \sim 7.0 \times 10^{20}$ cm^{-2}) with a size threshold of 300 pix^2. The masks were reduced to skeletons using medial axis transform, which extracts one single filament. A single filament of ~1.2 pc in length that runs throughout the coma-structure of the cloud is traced. For the purpose of analysis, we divided the filament into east-west and north-south segments. The orientation of the east-west segment is found to be 77°and a curvature of 76° with respect to the north increasing eastward. The extracted filament is shown in Figs. 1 and 3.

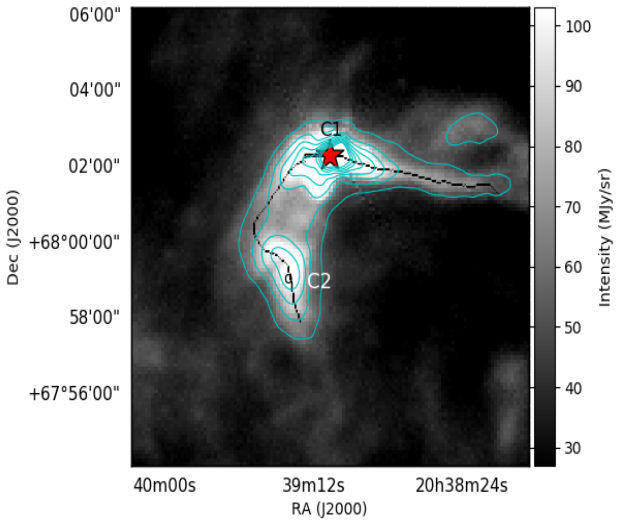

Fig. 3. Contours of the column density, N(H_2), in cyan overlaid on the *Herschel* 250 μm grayscale emission. The red star represents the position of protostar as well as clump C1. The small black circle identifies the position of clump C2. The contours are shown from levels of 3–20σ ($\sigma \sim 7 \times 10^{20}$ cm^{-2}).

We used the well-known *Clumpfind* (Williams et al. 1994) routine to identify high-density regions in the filament from the column-density map. Based on the *Clumpfind* routine, we obtained two clumps: C1 and C2. They lie on the filament (Fig. 3). The centers of these clumps are 20h39m06.79s +68°02′12.27″ and 20h39m20.349s +67°59′03.74″ , with a typical uncertainty in the positions of ∼10″ (Fehér et al. 2017). Clump C1 is located on the east-west segment where the protostar L1157-mm is currently forming, and clump C2 is found to be located on the north-south segment of the filament. Based on the absence of any 70 μm source associated with C2, we classify it as starless. We note that if we had used a 250 μm emission map instead of the column density map, the *Clumpfind* algorithm would resolve C2 into two separate clumps. The reason may be that spatial resolution of the 250 μm emission map is higher than that of the column density map. Because our molecular line observations also detect a single-density peak at the position of C2 due to relatively coarse spatial resolution, we consider C2 as a single clump in our study.

The radial profiles and widths of the filaments are two of the most important properties of prime interest for understanding the dominant physics (gravity, turbulence, and magnetic field orientation) that are involved in their formation. We constructed the column density profiles of the filament identified in L1157 using the publicly available package *Radfil* (Zucker & Chen 2018). The derived filament mask and the spine of the column density map derived from *Filfinder* were supplied as input. The spine was smoothed to obtain a continuous distribution in column density. The crest of the filament was sampled at an interval of 40 pixels (0.18 pc), which corresponds to three times the beam width (0.061 pc at 340 pc). Therefore the mean profile was constructed by averaging the profiles of the perpendicular cuts made at nine positions along the filament and setting the *Fold* = *True* in the *Radfil* to add all the profiles toward positive radial distance. We fixed the fit distance from 0.0 to 0.5 pc and evaluated the background at a distance of 0.5–0.6 pc from the filament crest (out of all possible trials conducted using the *Radfil*, the minimum value of the background column density was estimated from this distance range). A zeroth-order polynomial fit was applied to the background subtraction before we made the fits to the profile. The diameter of the flat inner plateau is found to be $2\,R_{\rm flat}$ = 0.126 ± 0.003 pc. The observed mean column density profile was fit by a Gaussian model over the inner radius of 0.05 pc. The power-law index of the best-fit Plummer model is $p = 3.1 \pm 0.2$, while the mean deconvolved width of the best-fit Gaussian model is $FWHM = 0.09$ pc.

An elongated structure showing minimum values of both aspect ratio and column density contrast with respect to the background value is normally identified as a filament (Arzoumanian et al. 2019). The aspect ratio, defined as $l_{\rm fil}/W_{\rm fil}$, of the sole filament identified in L1157 is 1.2/0.09 ∼ 14. The intrinsic column density contrast, $N^o_{\rm H_2}/N^{\rm bg}_{\rm H_2}$, of the filament is estimated to be ∼8, where $N^o_{\rm H_2}$ (= $N^{\rm fil}_{\rm H_2}$–$N^{\rm bg}_{\rm H_2}$) is the column density amplitude of the filament. The column densities of the pixels that form the extracted filament structure were averaged to obtain a representative value for the whole filament. One of the important consequences of obtaining a column density profile is that the mass per unit length can be calculated. We derived the mass per unit length ($M_{\rm line}$) for each position along the filament using the best-fit Gaussian parameters: central column density ($N_{\rm H_2}$) and standard deviation (σ). The lower right panel of Fig. 4 shows the distribution of the background-subtracted Gaussian mass-per-unit length along the crest of the filament at every cut, which was taken at an interval of 3 pixels (∼0.015 pc). The dashed horizontal line marks the critical mass-per-unit length that characterizes an isothermal cylindrical filament in equilibrium. The extreme end of the north-south segment of the filament (20h39m17s +67d57m56s) was taken as the starting point of the filament. The upper right panel in Fig. 4 shows the deconvolved FWHM derived from the Gaussian fitting of the mean column density radial profile as a function of distance along the filament crest. Although the cloud reflects as a single filament derived from the *Filfinder* algorithm, differences are found in the inner widths of the north-south and the east-west branches. The characteristic width of the east-west branch is better defined and constrained than that of the north-south branch. The positions for which we were unable to fit the radial profile with a well-defined Gaussian function are not included in the plot. The small dip near C2 corresponds to the region between the two peaks seen in the 250 μm *Herschel* map (*FWHM* ∼18″,) but which are barely noticeable in the column density map (*FWHM* ∼36″).

3.3. Molecular line analysis

The CO isotopologs are commonly used to probe the gas at different densities. While the most abundant isotopolog, ^{12}CO is considered to trace the most diffuse and external gas of molecular clouds, its rarer counterpart, the C^{18}O (J = 1–0) line with its critical density of 2.4×10^4 cm^{-3}, is one of the best tracers of high column- and volume densities without becoming saturated. However, C^{18}O is found to disappear from the gas phase in high chemically evolved regions because it condenses onto the surface of the dust grains (Caselli et al. 1999; Bergin et al. 2002; Cazaux et al. 2017). The N_2H^+ molecular line, on the other hand, is considered to be the most efficient tracer of dense cores in clouds because the abundance of this molecule becomes enhanced when CO condenses onto the dust grains (Bergin & Tafalla 2007).

The kinematic information from the observed molecular lines was extracted by fitting Gaussian profiles to all our spectra using programs developed in Python. We examined an individual spectrum and fit it independently using one single component at each individual position in C^{18}O lines. We obtained a total of

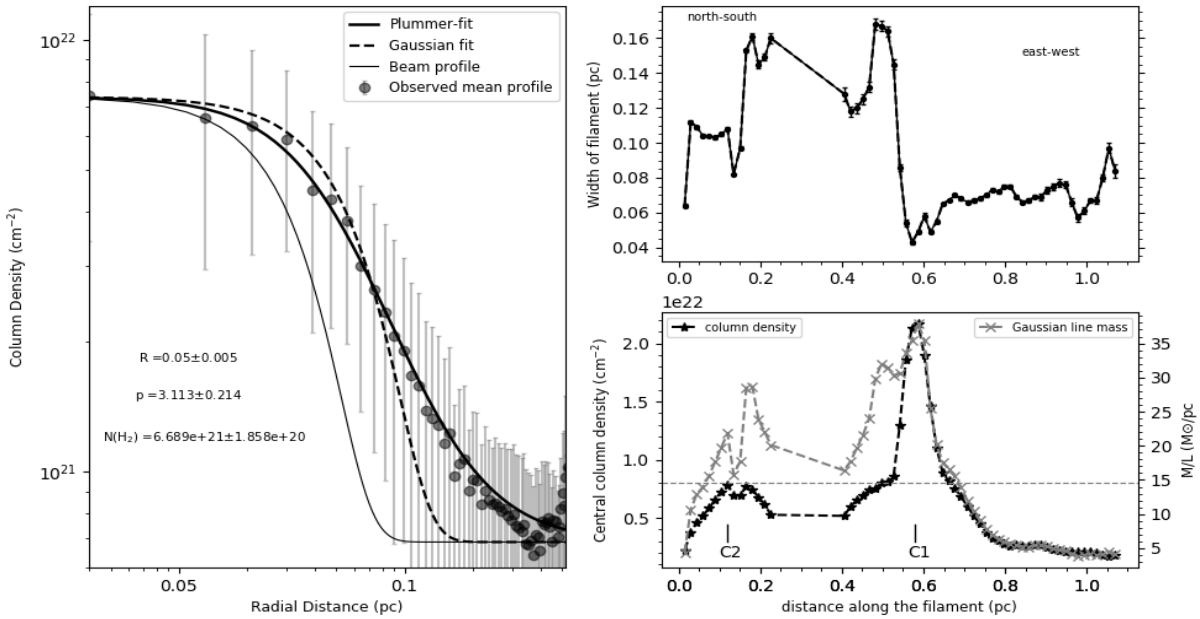

Fig. 4. *Left panel*: mean radial column density profile of the L1157 filament (gray points) measured perpendicular to the crest of filament shown in Fig. 1. The gray error bars mark the $\pm 1\sigma$ dispersion of the distribution of radial profiles along the spine of the filament. The solid black curve shows the best-fit Plummer model fitted on the mean radial profile. The black dashed curve marks the best-fit Gaussian function to the inner radius of the profile. The thin solid black curve represents the Gaussian profile of the beam. *Right upper panel*: deconvolved Gaussian FWHM of the L1157 filament as a function of position along the crest of the filament (starting from southern core toward the central protostar). *Right lower panel*: the central column density along the crest of the filament obtained from the best-fit Plummer model is plotted as the dashed black line. Background-subtracted mass-per-unit length calculated from the Gaussian fit (dashed gray line). The dashed gray horizontal line indicates the critical mass-per-unit length or line mass of an isothermal filament in equilibrium as $2c_s^2/G \sim 15\ M_\odot\ \mathrm{pc}^{-1}$ at 10 K.

1089 spectra in ^{12}CO and C^{18}O and 306 spectra in the N_2H^+ lines from the field containing the cloud L1157.

Various fundamental properties of the cloud like excitation temperature, optical depth, and the number density were derived using spectral data obtained at different positions of the cloud. Two assumptions were made to estimate the column density (N_{18}) based on the C^{18}O and ^{12}CO lines: the molecules along the line of sight possess a uniform excitation temperature for the $J = 1{-}0$ transition, and the $J = 1{-}0$ excitation temperatures of the two isotopic species are equal (e.g., Dickman 1978; Sato et al. 1994). The emission from the ^{12}CO molecule is optically thick, and the common excitation temperature (T_{ex}) was calculated from the peak ^{12}CO brightness temperature using the expression $T_b = T_R^{12}/\eta_{eff}$, where η_{eff} is the beam efficiency of the TRAO telescope. The brightness temperature, T_b^{12}, is calculated as,

$$T_b^{12} = T_0^{12}[f_{12}(T_{ex}) - f_{12}(2.7)], \tag{4}$$

where T_0^{12} is the temperature corresponding to the energy difference between the two levels given by $T_0^{12} = h\nu_{12}/k$, here ν_{12} is the frequency for $J = 1{-}0$ transition. In the same manner, the optical depth of the C^{18}O line (τ_0^{18}) was also calculated from the peak brightness temperature and the excitation temperature (T_{ex}) using the expression,

$$T_R^{18} = T_0^{18}[f_{18}(T_{ex}) - f_{18}(2.7)][1 - \exp(-\tau_0^{18})]. \tag{5}$$

The column density along the line of sight was calculated as,

$$N_{18} = \frac{3h\triangle v_{18}}{8\pi^3\mu^2}\frac{\tau^{18}Q}{\left[1 - \exp -\frac{T_0}{T_{ex}}\right]}, \tag{6}$$

where Δv_{18} is the line full width at half-maximum in velocity units, μ is the permanent dipole moment of the molecule, h is the Planck constant, and Q is the partition function. Again an assumption was made regarding the partition function, which depends upon the excitation temperatures of all significantly populated states of the molecule such as,

$$Q = 1 + \sum_{L=1}^{+\infty}(2L+1)\prod_{J=0}^{L}\exp[-h\nu(J)/kT_{ex}(J)], \tag{7}$$

where $\nu(J)$ and $T_{ex}(J)$ are the frequency and excitation temperature of the transition $J = 1{-}0$, respectively. This means that we assumed that all the levels have the same T_{ex}. The partition function can be written as $Q = \frac{2T_{ex}^{18}}{T_0^{18}}$. Not all the lines were fit to a perfect Gaussian, however. We therefore used the chi-square minimization to determine the goodness-of-fit. We obtained integrated intensity (moment 0) maps of ^{12}CO and C^{18}O using spectral data cubes with position-position velocity information. The values below 3σ were not considered to obtain summation over the channels. The rms value of each line map was calculated as $\sim \sqrt{N}\delta v T_{rms}$, where N is the number of channels used for integrating the emission, δv is the velocity resolution, and T_{rms} is the noise of the line profile.

The characteristic shape of the observed line profiles is a critical factor in determining the physical state of molecular gas in a region. Figure 5 in the left-hand panel shows the ^{12}CO and C^{18}O (1–0) line profiles plotted together at different positions in the cloud, and the right-hand panel shows the average ^{12}CO, C^{18}O, and N_2H^+ (isolated component) profiles over the half-maximum contour of the intensity map of N_2H^+ emission. The ^{12}CO emission is detected throughout the observed region and conspicuously shows diverse line profiles with an asymmetric

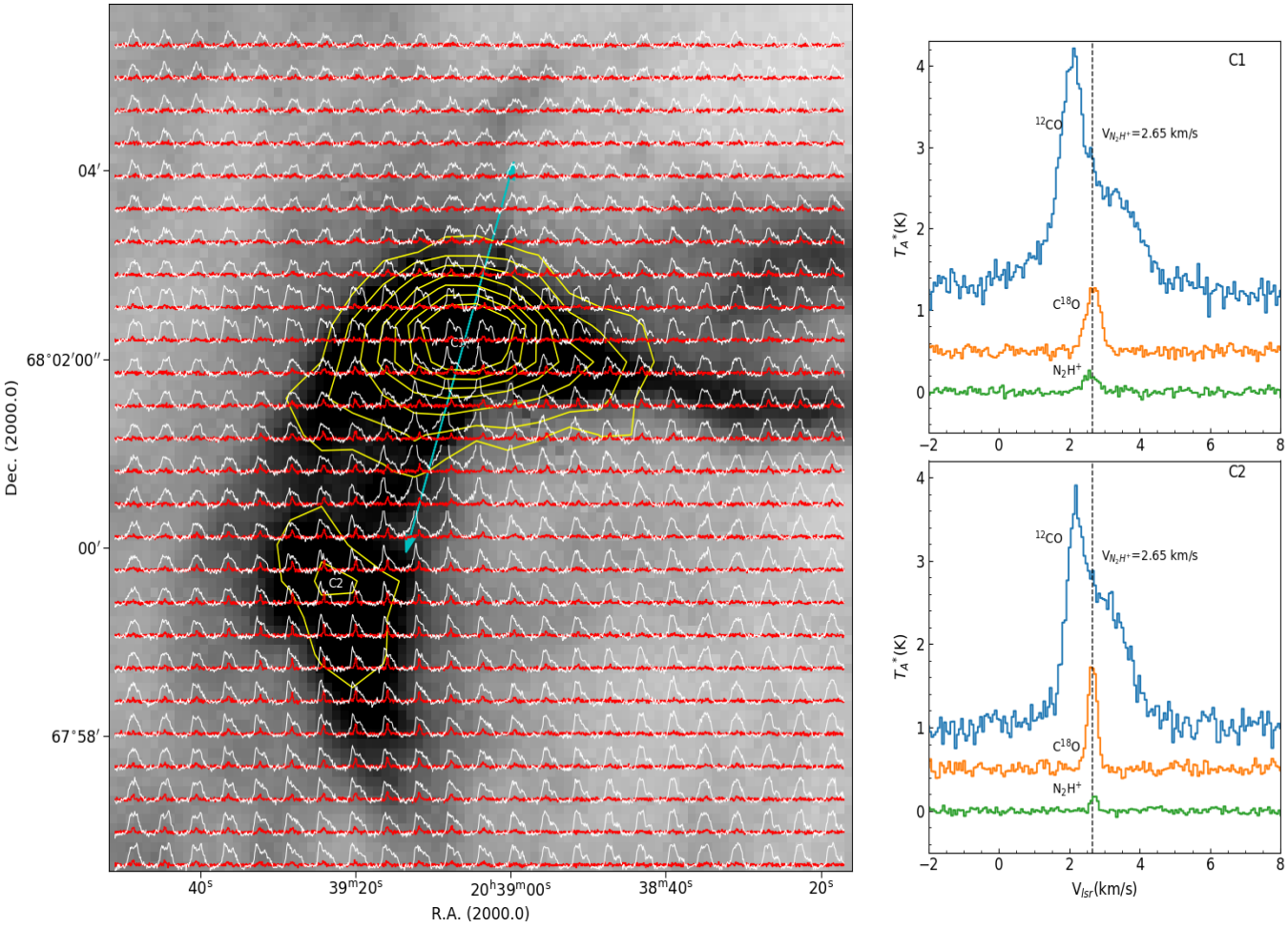

Fig. 5. Distribution of ^{12}CO (white) and C^{18}O (red) profiles over the 9′ × 9′region. In the *left-hand panel*, the background image is the *Herschel* 250 μm emission for cloud L1157, on which we overlay contours of the N_2H^+ (1–0) line in yellow. The positions of core C1 and clump C2 are marked in white. The extent of the outflow is marked by the cyan arrow. Contour levels start from 4σ in steps of 3σ, where $\sigma \sim 0.05$ K km s^{-1}. The small windows in the *right-hand panel* show the average spectra of the ^{12}CO, C^{18}O, and N_2H^+ (1–0) (isolated component) lines for C1 (*top*) and C2 (*bottom*). The average was taken over the half-maximum contour of the intensity map of the N_2H^+ emission for C1 and C2. The dashed line indicates the velocity of N_2H^+ obtained from the Gaussian hyperfine fitting of its seven hyperfine components.

structure detected in a large area. The ^{12}CO lines show a wide line width and two velocity components especially in the cloud. This might either be due to self-absorption by the optically thick material at the systematic velocity of the cloud, if there is only a single cloud component, or to additional velocity components along the line-of-sight. The significant emission of the C^{18}O line ($\geq 3\sigma$) was obtained toward the high column density region seen in the *Herschel* dust map, as shown in Fig. 3. The C^{18}O line profiles show an optically thin feature, that is, a single Gaussian component. The absorption of the double-peaked profiles of ^{12}CO lines coincides with the single peak of C^{18}O emission, confirming that there is only a single cloud component along the line of sight.

The C^{18}O line width is found to be much narrower than that of ^{12}CO. The well-studied outflow (Umemoto et al. 1992) is evident as broad high-velocity wings on either side of the ^{12}CO line profiles when compared visually with the shape of the C^{18}O Gaussian component. Interestingly, at many positions along the filament and in surrounding regions around C1 and C2, the profiles show a blue-red asymmetry (Sect. 4.5). The N_2H^+ emission is detected toward both C1 and C2.

4. Discussion

4.1. Distance of the L1147/1158 complex

One of the most direct methods of determining distances to molecular clouds is estimating distances of the YSOs that are associated with the cloud (e.g., Loinard et al. 2007; Ortiz-León et al. 2018). The stellar parallax measurements obtained for these YSOs from the *Gaia* DR2 (Lindegren et al. 2018) offer an unprecedented opportunity to estimate distances to molecular clouds with improved accuracy and precision. A total of six YSO candidates have been identified so far toward the direction of L1147/1158 (Kun 1998; Kirk et al. 2009). We found a *Gaia* counterpart for three of the six YSO candidates well within a search radius of 1″. The *Gaia* results are presented in Table 2. We obtained their distances from the Bailer-Jones et al. (2018) catalog, and proper motion values in right ascension ($\mu_{\alpha\star} = \mu_\alpha \cos\delta$) and in declination ($\mu_\delta$) from the Gaia Collaboration (2018) catalog. Within the L1147/1158 complex (Yonekura et al. 1997), the dark cloud L1155 harbors two YSOs, 2MASSJ20361165+6757093 and IRAS 20359+6745. Cloud L1158 hosts at its north-east edge an another YSO candidate, PV Cephei. The bright nebulosity associated with IRAS

Table 2. *Gaia* results of YSOs associated with the L1147/1158 and L1172/1174 complexes.

Source name	RA	Dec	l	b	Distance	μ_α	$\Delta\mu_\alpha$	μ_δ	$\Delta\mu_\delta$
	(°)	(°)	(°)	(°)	(pc)	(mas yr−1)	(mas yr−1)	(mas yr−1)	(mas yr−1)
(1)	(2)	(3)	(4)	(5)	(6)	(7)	(8)	(9)	(10)
L1147/1158 complex									
2MASS J20361165+6757093	309.048672	67.952608	102.4221	15.9738	336^{20}_{-22}	7.436	0.351	−1.514	0.284
IRAS 20359+6745	309.082855	67.942131	102.4205	15.9573	343^{12}_{-13}	7.753	0.189	−1.469	0.143
PV Cep	311.474902	67.960735	102.9697	15.2315	341^{6}_{-7}	8.228	0.126	−1.976	0.110
L1172/1174 complex									
FT Cep	314.845315	68.245467	103.9926	14.4053	339^{4}_{-4}	7.333	0.087	−1.599	0.079
2MASS J21002024+6808268	315.084447	68.140772	103.9661	14.2704	341^{9}_{-10}	7.630	0.147	−1.182	0.158
2MASS J21005550+6811273	315.231481	68.190885	104.0418	14.2596	332^{12}_{-13}	7.205	0.184	−1.649	0.280
NGC 7023 RS 2	315.359984	68.177338	104.0621	14.2140	325^{6}_{-6}	7.652	0.104	−1.416	0.121
NGC 7023 RS 2B	315.362884	68.177214	104.0627	14.2131	360^{12}_{-13}	6.667	0.174	−0.865	0.189
2MASS J21013583+6813259	315.399160	68.223752	104.1087	14.2321	277^{27}_{-33}	11.343	0.673	−3.039	0.706
LkHα 425	315.400352	68.139576	104.0418	14.1785	332^{6}_{-6}	6.971	0.106	−1.638	0.117
HD 200775	315.403923	68.163263	104.0616	14.1924	357^{5}_{-5}	8.336	0.079	−1.566	0.083
NGC 7023 RS 5	315.427117	68.215960	104.1093	14.2191	323^{8}_{-8}	7.530	0.148	−0.668	0.164
FU Cep	315.444875	68.145894	104.0577	14.1696	335^{4}_{-4}	7.770	0.071	−1.428	0.078
FV Cep	315.558650	68.233141	104.1549	14.1923	321^{25}_{-30}	8.666	0.528	−1.736	0.568
LkHα 275	315.584980	68.423341	104.3129	14.3056	277^{19}_{-22}	7.262	0.483	−3.589	0.530
LkHα 428 N	315.617758	68.058287	104.0301	14.0642	343^{6}_{-6}	6.868	0.098	−1.319	0.107
LkHα 428 S	315.618244	68.057669	104.0297	14.0637	376^{15}_{-16}	8.041	0.193	−1.202	0.215
FW Cep	315.637634	68.124746	104.0878	14.1008	336^{2}_{-2}	7.054	0.044	−1.017	0.043
NGC 7023 RS 10	315.747855	68.108939	104.1022	14.0590	323^{4}_{-4}	7.174	0.079	−1.738	0.075
2MASS J21025963+6808119	315.748555	68.136623	104.1244	14.0765	401^{85}_{-148}	5.678	0.849	−11.026	1.196
EH Cep	315.851719	67.985134	104.0295	13.9501	326^{7}_{-7}	7.269	0.140	−2.330	0.128
2MASS J21034154+6823456	315.923249	68.396018	104.3729	14.1922	559^{127}_{-230}	5.407	0.780	−3.269	0.752
2MASS J21035938+6749296	315.997585	67.824847	103.9389	13.8053	346^{8}_{-8}	7.722	0.152	−2.061	0.133

20359+6745 (Magakian 2003) and PV Cephei (Scarrott et al. 1991) are clear evidence of their association with their respective clouds. No detection was found in the *Gaia* DR2 database for the other three YSO candidates, L1148-IRS, which is associated with L1148 (Kun 1998), IRAS 20353+6742, which is associated with L1152 (Benson et al. 1988), and L1157-mm in L1157.

The mean value of the distance calculated from the three YSOs is 340 pc with a dispersion of 3 pc. The mean (standard deviation) values of the $\mu_{\alpha\star}$ and μ_δ for them are 7.806 (0.326) mas yr^{-1} and −1.653 (0.229) mas yr^{-1}, respectively. Similar distance and proper motion values shown by all the three YSOs indicate that they are spatially and kinematically associated with each other and that the complex is also located at a distance of 340 ± 3 pc from us. Similar values of $V_{\rm lsr}$ (∼2.6 km s^{-1}) shared by the individual clouds of the complex (Harjunpaa et al. 1991; Yonekura et al. 1997; Suzuki et al. 2014) also support this argument. Straizys et al. (1992), based on Vilnius photometry, which gives two dimensional classifications and the extinction suffered by the stars, estimated distances to the L1147/1158 cloud complex. Using ten reddened stars in the direction of L1147/1158, the authors estimated a distance of 325 ± 13 pc to the cloud.

The degree of P% measured in the optical wavelengths made using the pencil-beam of starlight passing through the interstellar medium is often found to correlate with the extinction ($A_{\rm V}$) measured to that line of sight up to at least an $A_{\rm V}$ of ∼3 magnitudes (Guetter & Vrba 1989; Harjunpää et al. 1999). As the distance to the observed stars increases, the column of the dust grains present along the pencil-beam therefore also increases, leading to a gradual increase in the P% if no significant depolarization occurs along the path. When the starlight passes through a molecular cloud, the measured P% will receive additional contribution from the dust grains present in it. This will lead to a sudden increase in the values of P% for the stellar background to the cloud, while the foreground stars will show P% due to the contribution from the foreground interstellar medium (ISM) alone. The presence of a molecular cloud can therefore be inferred from the measured polarization of the foreground and background stars (e.g., Cernis 1987; Guetter & Vrba 1989; Arnal et al. 1993; Rizzo et al. 1998; Alves & Franco 2007; Neha et al. 2016).

In Fig. 6 we show P% for the 62 stars observed by us as a function of their distances, which were obtained from the Bailer-Jones et al. (2018) catalog by searching for the *Gaia* counterparts within a search radius of 1″. For all the sources, we found a counterpart well within 1″ from our input coordinates. The sources selected from the Heiles (2000) catalog are also shown. The distances for these stars were also obtained from the Bailer-Jones et al. (2018) catalog. Up to a distance of ∼340 pc, the P% of sources obtained from the Heiles (2000) catalog show very low values. The weighted mean values of P% and $\theta_{\rm P}$ for the sources located at distances ⩽340 pc are 0.1 ± 0.05 and 65° ± 29°, respectively. For the four sources located beyond

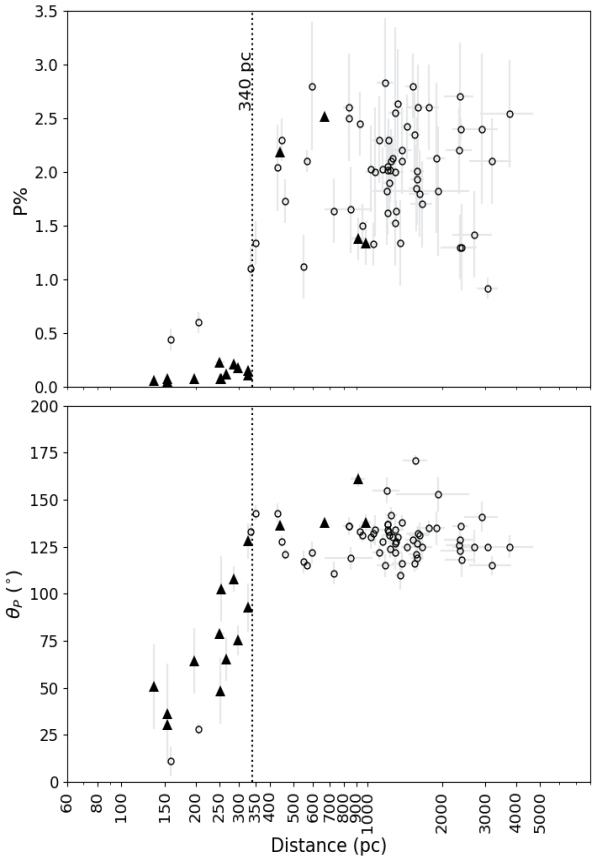

Fig. 6. *Upper panel*: P% vs. distance of the sources for which we made polarization measurements (open black circles). The distances are obtained from the Bailer-Jones et al. (2018) catalog. Polarization measurements of the field stars (filled triangles) are obtained from the Heiles (2000) catalog. The vertical line is drawn at 340 pc. *Lower panel*: variation of polarization position angles of stars as a function of their distances.

340 pc, the weighted mean values of P% and θ_P are found to be 1.6 ± 0.4 and $148° \pm 11°$, respectively. The θ_P of the sources from the Heiles (2000) catalog are found to show a systematic change from ∼25° to ∼125° with distance until about 340 pc. Beyond this distance, sources are found to show θ_P similar to those obtained for our target sources. Only two of the sources observed by us have distances smaller that 340 pc. The weighted mean values of P% and θ_P of these two sources are 0.5 ± 0.1 and $16° \pm 8°$, respectively. For the sources observed by us and located at or beyond 340 pc, the weighted mean values of P% and θ_P are found to be 2.1 ± 0.6 and $129° \pm 11°$, respectively. The distribution of P% and θ_P as seen in Fig. 6 further supports the 340 pc distance estimated for the L1147/1158 cloud complex.

4.2. Magnetic field geometry in L1157

The dynamics of interstellar dust grains can be affected by the presence of a magnetic field. It was shown that rotating non-spherical dust grains would tend to align with their long axis perpendicular to the interstellar magnetic field (Davis & Greenstein 1951; Jones & Spitzer 1967; Purcell 1979; Lazarian 1995; Crutcher 2012). When unpolarized starlight from a background star passes through regions of such aligned dust grains, they polarize the starlight by selectively absorbing the component parallel to the long axis of the grains. Thus the polarization position angles provide a sense of the plane-of-sky component of the magnetic field. As it is evident that most of the stars observed by us toward L1157 are background stars, the measured values of θ_P represent the magnetic field geometry of the cloud. The two stars in our sample that are foreground stars show higher P% values than those from the Heiles (2000) catalog. We subtracted the mean P% and θ_p values of these two foreground sources from the remaining sources vectorially and found the values to be 2.3 ± 0.8 and $127° \pm 12°$. Therefore, $127° \pm 12°$ was taken as the orientation of the magnetic field in L1157 inferred through optical polarization. The magnetic field orientations thus obtained are overplotted on the DSS image as shown in Fig. 7a. The position of the protostar L1157-mm is shown as well. The length of the vectors corresponds to the P% values and the orientations correspond to the θ_P values measured from the north, increasing toward the east. The polarization measurements using background starlight in the optical wavelengths typically only hold for the regions of low A_V ($\lesssim$5). This is because although the dust grains deep inside the molecular clouds are efficient in diminishing background starlight, they are believed to be little efficient in polarizing the light in optical wavelengths (Goodman et al. 1995; Crutcher 2012). Therefore the optical polarization vectors shown in the Fig. 7a basically trace the orientation of the magnetic fields at the envelope (low-density regions) of L1157. The magnetic field orientation is found to be well ordered at ∼0.2−2 pc scales, which suggests that the intercloud magnetic field (ICMF) might have played an important role at least in the initial building up of the cloud.

The magnetic field orientation of a region can also be inferred through the observations of polarized thermal emission from the dust grains (Hildebrand et al. 1984; Goodman 1995; Greaves et al. 1999). Far-infrared and submillimeter polarimetric observations made by the *Planck* were used not only to infer the direction of the Galactic magnetic field, but also to place new constraints on the properties of dust (Planck Collaboration Int. XXI 2015; Planck Collaboration Int. XXXII 2016; Planck Collaboration Int. XXXV 2016)[1]. We used the 353 GHz (850 μm) data. The 353 GHz channel is the highest-frequency polarization-sensitive channel of the *Planck*. We produced the structure of the Galactic magnetic field in the vicinity of L1157 based on these data. We selected an image with a diameter of ∼1° centered on the cloud and smoothed it down to the 8′ resolution to obtain a good S/N. The results are shown in Fig. 2 using dots in gray. The P values range from ∼2–8% with a mean value of 4.4% and a standard deviation of 1.6%. The dust emission is linearly polarized with the electric vector normal to the sky-projected magnetic field, therefore the polarization position angles were rotated by 90° to infer the projected magnetic field. The polarization position angles show a highly regular distribution with a mean value of 127° and a standard deviation of 6°. The polarization vectors are presented in the $0.5° \times 0.5°$ DSS image, as shown in Fig. 7a. The vectors in blue are those from a $0.3° \times 0.3°$ circular region similar to where we carried out optical polarization observations. These results are shown in Fig. 2 using filled squares in black. We note that the positions showing relatively higher values of P show a relatively lower dispersion in θ_P. The mean and standard deviation of the source with $P \geqslant 4\%$ are 129° and 4°, respectively. The projected magnetic field geometry inferred from the optical and the *Planck* polarimetry agrees

[1] The entire sky was surveyed by the *Planck* in nine frequency bands, from 30 to 857 GHz, with unprecedented sensitivity, and angular resolutions varying from 30′ at 30 to 4.8′ at 857 GHz. Seven of the nine bands were sensitive to polarized thermal emission from Galactic dust.

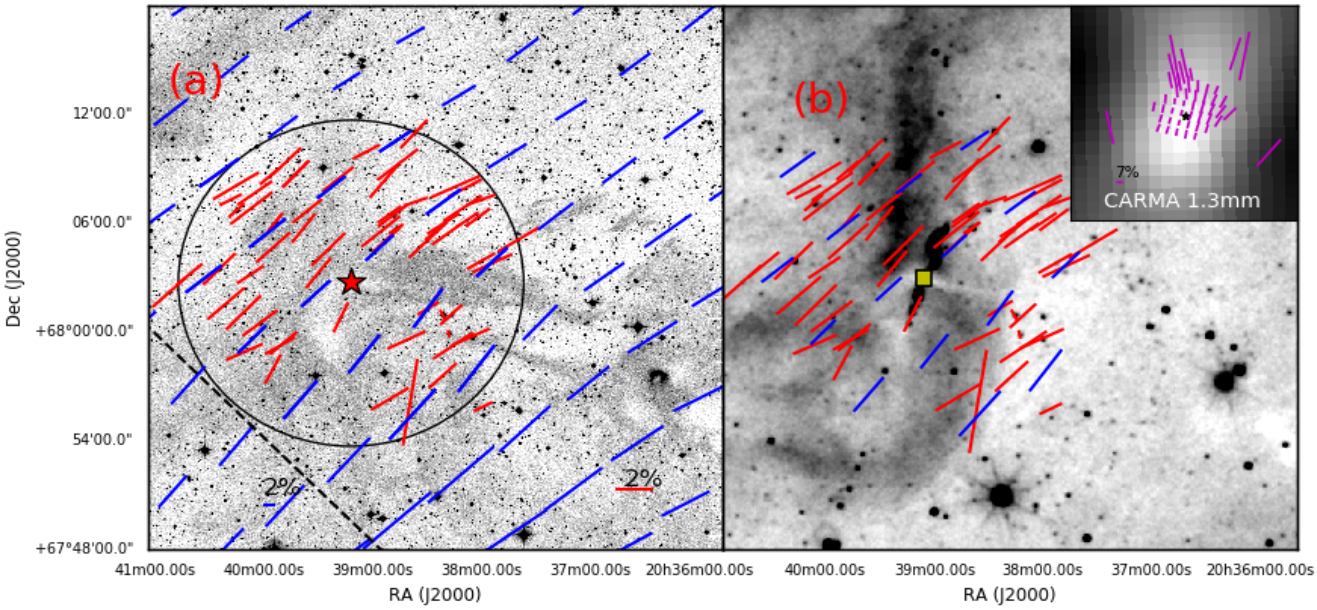

Fig. 7. (*a*) Optical polarization vectors (in red) overplotted on the $0.5° \times 0.5°$ DSS image. The dashed line shows the direction of the Galactic plane. The circle shows the region of optical polarization observations. *Planck* polarization vectors are shown in blue (inside and outside the circle). (*b*) WISE 12 μm image for the same region in inverted scale. Optical (in red) and *Planck* (in blue) polarization vectors are overlaid. The yellow box around the location of the protostar marks the region of submillimeter polarization observations observed in wavelength 1.3 mm using CARMA (Hull et al. 2013), and the vectors are shown in the inset (upper right corner) in magenta. The location of the protostar in the inset is identified by the black star.

well. An agreement like this between the magnetic field directions inferred from the optical and *Planck* is observed toward a number of clouds belonging to the Gould Belt (Soler et al. 2016; Gu & Li 2019).

4.3. Magnetic field strength

We used the Davis-Chandrasekhar & Fermi (DCF) (Davis 1951; Chandrasekhar & Fermi 1953) method to estimate the plane-of-the-sky magnetic field strength of L1157. The DCF method is formulated as

$$B_{\rm pos} = 9.3 \times \sqrt{\frac{n_{\rm H_2}}{\rm cm^{-3}}} \times \frac{\Delta v}{\rm kms^{-1}} \times \left(\frac{\Delta\phi}{1°}\right)^{-1}, \quad (8)$$

where Δv is the FWHM of the CO(1–0) line, which is measured as $\sim$1.8 km s^{-1}. We used only those lines to measure FWHM that can be fit with a single Gaussian function. Here $n_{\rm H_2}$ is the volume density of L1157, which is found to be 1000 cm^{-3}. To calculate the volume density, we used a column density of 8.0×10^{20} cm^{-2} and a depth of the cloud of 0.3 pc. We considered the extent of the column of the cloud material lying along the line of sight as three times the width of the filament, which is about 0.1 pc. In the equation, $\Delta\phi$ is dispersion in the distribution of polarization position angles, which is measured as 11°. The magnetic field strength in the envelope of L1157 is found to be $\sim$50 μG. By propagating the uncertainties in measured position angle and velocity dispersion values, we calculated the uncertainty in the magnetic field strength as $\sim 0.5\, B_{\rm pos}$. The field strength in the dense core region of L1157 has been reported to be 1.3–3.5 mG by Stephens et al. (2013) using their 1.3 mm dust continuum polarization observations. These values are about two magnitudes higher than our measurements, which suggests that the core has stronger magnetic fields than the envelope of L1157.

4.4. Correlations between magnetic field, filament, and outflow directions in L1157

The star formation process begins with the accumulation of matter from the ICM. In models where magnetic fields are dynamically more important than turbulence (e.g., Shu et al. 1987; Galli & Shu 1993a,b; Tomisaka 1998; Allen et al. 2003a,b), the accumulation of matter is controlled by the ICMF. The gas slides along the field lines (Ballesteros-Paredes et al. 1999; Van Loo et al. 2014), forming filamentary structures that are aligned perpendicular to the ICMF. In these filaments, cores are found to be forming (Polychroni et al. 2013; Könyves et al. 2015). Because the assembly of matter is guided by the magnetic fields, the ICMF direction is expected to be preserved deep inside the cores (Li et al. 2009; Hull et al. 2014; Li et al. 2015), predicting the ICMF to become parallel to the core magnetic field (CMF). The local CMF within individual cores (subcritical) provides support against gravity, preventing them from collapsing and thus accounts for the low efficiency of the star formation process (e.g., Mouschovias 2001). The neutral particles, coupled weakly to the ions and hence to the magnetic fields, can drift toward the center of the core, enabling it to amass more material. The increasing central mass gradually increases the mass-to-magnetic flux ratio, leading the core to become supercritical and driving it to collapse under gravity. Under the influence of gravity, the initial uniform magnetic field is expected to be dragged toward the center of the core, forming an hourglass-shaped morphology (Galli & Shu 1993a,b). As the collapse progresses, a pseudo-disk is expected to form in the central region with the symmetry axis of the pinching perpendicular to it. The protostellar object embedded deep inside the cores continues to build up mass through accretion and simultaneously develops a bipolar outflow. Because the initial cloud angular momentum is expected to be hierarchically transferred to the cores and eventually to the protostar, the rotation axis (of the core or accretion disk) is

expected to become parallel to the ICMF and CMF (Machida et al. 2006; Matsumoto et al. 2006) and perpendicular to the core minor axis and the filament structure.

In this framework of magnetic field-mediated star formation, a number of observational signatures that show the role played by the magnetic fields are detected (e.g., Li et al. 2009, 2015; Hull et al. 2014). Some of these are (i) the relative orientations between (a) the ISMF and the CMF, (b) the ISMF and the long axis of the filament, (c) the ISMF, CMF, and bipolar outflows, (d) the filament and the outflows, and (ii) the hourglass morphology of the magnetic field at the core scale with the symmetry axis perpendicular to the major axis of the flattened pseudo-disk. We examined these relationships in L1157, which is not only successful in forming a star ,but is also at its earliest stages of star formation, therefore the initial conditions that led this cloud to form star may still be conserved.

The polarization measurements of the region surrounding L1157-mm were carried out at 1.3 mm (resolution 1.2″–4.5″) and 350 μm (10″) (Chapman et al. 2013; Stephens et al. 2013) with the aim to trace the magnetic field orientation in the inner regions of the core (Hildebrand et al. 1984; Goodman 1995; Greaves et al. 1999). The SHARP and CARMA vectors with their standard deviation have been quoted as $P = 0.7\% \pm 0.2\%$ and θ =142° ± 9°, and $P = 3.8\% \pm 0.1\%$ and θ =147.8° ± 0.8°, respectively. We adopted an orientation of 145° ± 9° for the CMF, which is the mean value of the magnetic field directions inferred from the SHARP and CARMA results. The magnetic field inferred from the 1.3 mm polarization measurements is shown in the inset in Fig. 7b by overplotting the vectors on the WISE 12 μm image. The CARMA and SHARP polarization measurements were carried out at scales of ∼400−1500 au and ∼3500 au (using the distance of 340 pc), respectively, thus representing the CMF. The offset between the relative orientations of the ICMF inferred from the optical (and the *Planck*) polarimetry and the CMF obtained from the SHARP and CARMA is ∼18° ± 14°. The nearly parallel orientations of ICMF and CMF suggest that the CMF is anchored at the ICMF in L1157. The near parallel magnetic field geometry from large to core scales indicates that the fields have not been disturbed by turbulent motions resulting from the collapse of material during the star formation process in L1157.

The orientation of the magnetic field toward L1157-IRS was found to exhibit an hourglass morphology (Stephens et al. 2013). The symmetry axis of the hourglass morphology is found to be perpendicular to a flattened structure (∼0.1−0.2 pc) seen in absorption against bright emission, possibly due to the polycyclic aromatic hydrocarbons from the diffuse interstellar medium in the background (Looney et al. 2007). The N_2H^+ emission, having a spatial extent of ∼30 000 au and oriented 75° north to east (elongated perpendicular to the outflow; Chiang et al. 2010), is found to coincide with the absorption feature. These structures extend farther, at least at the western side of L1157-mm, and coincide with the east-west segment of the filament up to a length of ∼0.5 pc. According to the *Filfinder* algorithm, the east-west segment of the filament is oriented at an angle of 79° (consistent with the orientation of N_2H^+ emission) and makes an offset of 48° with respect to the ICMF and of 66° with respect to the CMF direction. The offset of 66° to the CMF with respect to the east-west segment of the filament suggests that the star formation in L1157 supports a scenario where the magnetic field is sufficiently strong enough to have influenced the formation of at least the east-west segment of the filament structure (Soler et al. 2013; Planck Collaboration Int. XXXV 2016). An alternative possibility for the formation of the east-west segment is discussed in Sect. 4.7. The north-south segment of the filament, however, is found to be almost parallel to the ICMF and CMF.

The relative orientation of the bipolar outflow and the filament (the absorption feature and the N_2H^+ emission) in L1157 is found to be 82° ± 10° (assuming an uncertainty of 10° in the determination of the outflow position angles, e.g., Soam et al. 2015), which means they lie almost perpendicular to each other. When we consider the outflow direction as a proxy for the rotation axis, then the orientation of outflow with respect to the filament provides evidence for the manner in which matter was accumulated prior to the initiation of the star formation. In L1157, the material might have first become accumulated onto the filament channeled by the magnetic field lines aligned perpendicular to it, and then, as the density increased, the flow pattern changed direction and might have flown along the filament toward the core. In this scenario, we would expect the rotation of the protostar to be perpendicular to the filament because the local spin motion depends on the flow direction (Clarke et al. 2017; Stephens et al. 2017).

The offsets between ICMF and the outflow direction and between CMF and the outflow direction is 34° ± 16° and 16° ± 14° (see also Stephens et al. 2013), respectively, which suggests that the CMF is relatively more aligned with the outflow than the ICMF. Examples of alignment and misalignment or random alignment of outflows and magnetic field exist in the literature. Although studies have shown that the outflows are preferentially misaligned or are randomly aligned with the magnetic fields, L1157-mm shows a good alignment, especially between the directions of the outflow and CMF (see also Hull et al. 2013). Misalignments between magnetic fields and outflows are suggested as an essential condition to allow the formation of a circumstellar disk (Krumholz et al. 2013).

4.5. Properties of the matter along the filament

To study the dust properties and large-scale velocity field of the gas lying along the spine of the filament identified toward L1157, we derived the peak line temperature, velocity centroids, and velocity dispersion by making Gaussian fits to all $C^{18}O$ spectra with an $S/N \geqslant 3$. The results are presented in Fig. 8 as a function of the positions along the main axis of the filament. The southern end of the north-south segment of the filament is taken as the starting point. The positions of the two condensations C1 and C2 identified using the *Clumpfind* routine are marked. To compare the properties of dust and gas emission in the cloud, we convolved and regridded the dust column density map at ∼36″ grid using the beam size of TRAO (∼49″ at 110.20 GHz) (Jeong et al. 2019). The advantage of this approach is that the comparison is made over the same area on the source, but the disadvantage is that all the spatial structures smaller than this beam size are smoothed out.

In panels (a) and (b) of Fig. 8 we show the derived dust column density and the dust temperature calculated using the *Herschel* data along the filament. The column density ranges from 1.7×10^{21} to 1.3×10^{22} cm^{-2}. The average dust column density of the filament is $\sim 5 \times 10^{21}$ cm^{-2}. The dust temperature ranges from 12 to 15 K with an average temperature of 13 K. The column density and the dust temperature both peak at the position of L1157-mm. However, the values remain nearly constant in the north-south and east-west segments of the filament. The peak value of the dust column density in the filament, 1.3×10^{22} cm^{-2}, is found at the position of C1 where L1157-mm is embedded. The mass-per-unit length values along the length of the filament were derived using the radial profile analysis as shown in Fig. 4

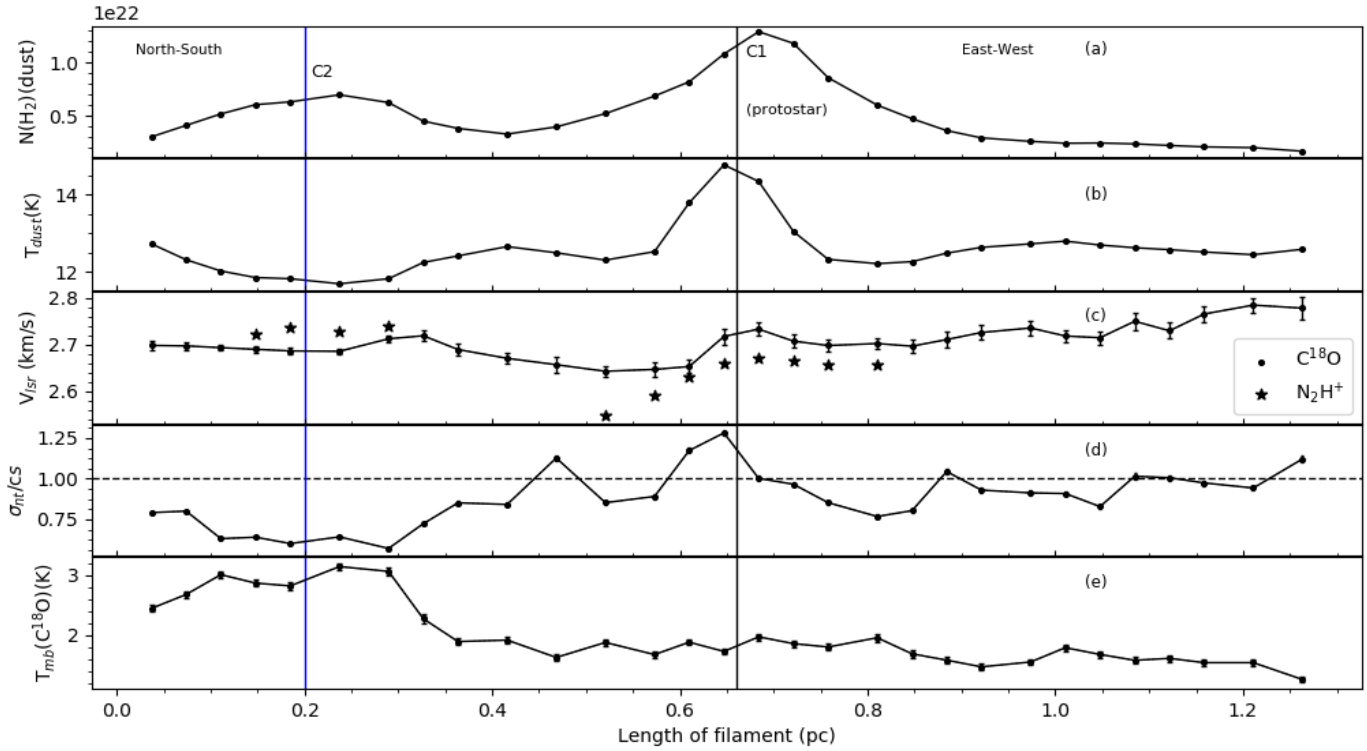

Fig. 8. Results of $C^{18}O$ (1–0) and dust emission analysis along the cloud filament length. (*a*) Hydrogen column density derived using *Herschel* PACS and SPIRE images. (*b*) Dust temperatures. (*c*) Centroid velocity of $C^{18}O$ obtained from Gaussian fitting of profiles (filled dots). The centroid velocities obtained using hyperfine fitting of the N_2H^+ (1–0) line coinciding with the positions along the filament are marked by filled stars. (*d*) Mach number, which is the ratio of the nonthermal velocity dispersion (σ_{nt}) along the line of sight and the isothermal sound speed (c_s) at 10 K (~0.19 km s^{-1}). The blue line at 0.2 pc and the black line at 0.65 pc show the position of clump C2 and the class 0 protostar L1157-mm, respectively. (*e*) Main-beam brightness temperature using $C^{18}O$ lines.

(right lower panel). Ostriker (1964) considered the mass-per-unit length or line mass of an isothermal filament in equilibrium as $2c_s^2/G \sim 15\ M_\odot\ pc^{-1}$ at 10 K. The mass-per-unit length along the filament in L1157 ranges from 4–38 $M_\odot$ pc^{-1}. The line masses around C1 and C2 are higher than the equilibrium value, which implies that these parts of the filament are supercritical. The values obtained around C1 and C2 are consistent with those found toward the Taurus molecular cloud (Palmeirim et al. 2013).

The mean column density profile of the L1157 cloud is described with a Plummer-like function with a power-law index of $p \sim 3$ (see Sect. 3.2). The value falls in the range of the typical values of p (~1.5–3) obtained in the case of several filaments, such as $p \sim 2.7$–3.4 in L1517 (Hacar & Tafalla 2011) and p = 3 in L1495 (Tafalla & Hacar 2015). The radial equilibrium of the filamentary clouds can be explained by considering them as isothermal cylinders using pure hydrostatic models (Ostriker 1964) or magnetohydrostatic models (Fiege & Pudritz 2000b). The former models can lead to density profiles as $\rho \sim r^{-4}$ and the latter ones to $\rho \sim r^{-2}$. Our results with the power-law index $p \sim 3$ suggest that the filament column density profile supports a theoretical model with magnetic fields. The results of magnetic field studies presented here support the hypothesis that the magnetic field has played an important role in the dynamical evolution of L1157.

$C^{18}O$ is detected at points all along the ~1.22 pc length of the filament and correlates well with the dust emission. The distribution of the ^{12}CO and $C^{18}O$ profiles all along the spine of the filament is shown in Fig. 9. Position 1 corresponds to the southern end of the north-west segment and position 30 corresponds to the western end of the east-west segment of the filament. There is a strong tendency that a blue asymmetry in the ^{12}CO line profile is seen in a high column density region, while no clear asymmetry in these lines is seen in the low column density region. The ^{12}CO line profiles at positions 1–3 in the north-south segment of the filament show a blue asymmetry. As we approach the C2 (positions 4–7), the ^{12}CO profile shows a blue-red asymmetry, with the blue peak brighter than the red peak. Then the line profile becomes more symmetric until position 12. The profile again shows a blue-red asymmetry as we approach C1 and continues until position 17. $C^{18}O$, which is an optically thin tracer, peaks at the velocity of the self-absorption, suggesting that the double-peaked profiles of ^{12}CO (Fig. 9 in panels 4–7 and 13–17) are most likely due to inward motions, assuming that the gas in the inner parts of C1 and C2 has a warmer excitation temperature than that toward the envelope. The inward motions seen here might be interpreted as due to collapse or infall motion (Lee et al. 1999, 2001; Tafalla et al. 1998). The linear extent of the infall motion is ~0.15 pc. The $C^{18}O$ lines are well fit with a Gaussian profile throughout the filament. The $C^{18}O$ line width around clump C2 is found to be narrower than that found around core C1. The ^{12}CO lines at positions 23–30 peaks at the systematic velocity of the cloud with an additional red component that is most likely caused by the effect of the red lobe of the outflow.

The values of the observed line width (FWHM) of the $C^{18}O$ profiles range from ~0.3 to 0.6 km s^{-1}. We fit a single Gaussian profile to all the $C^{18}O$ profiles and obtained the peak velocites. The mean value of V_{lsr} of the full L1157 filament was found to be 2.65 ± 0.05 km s^{-1}. The systematic velocity of the cloud was estimated by taking an average of the velocities at positions where significant emission in the N_2H^+ line

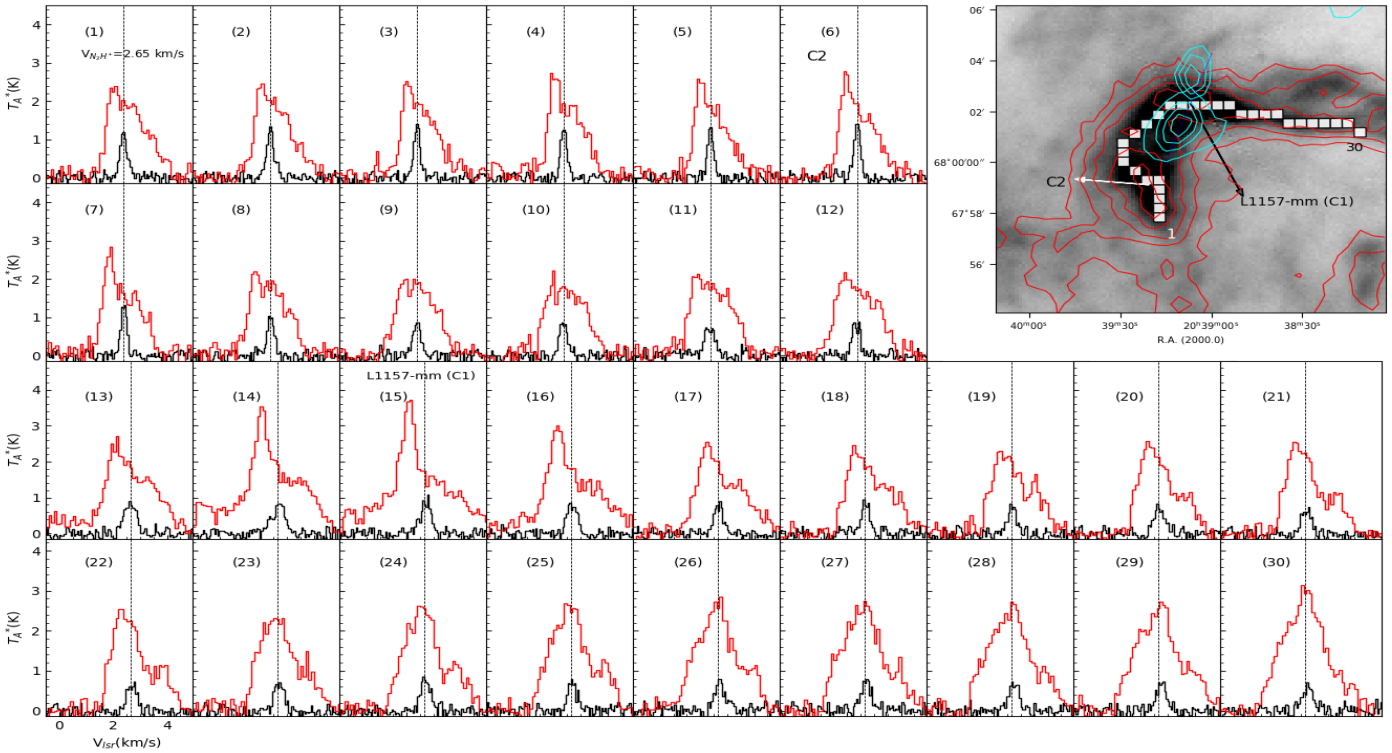

Fig. 9. Distribution of the $C^{18}O$ (black) and ^{12}CO (red) (1–0) line along the positions of the *Filfinder* skeleton. The dotted line shows the v_{lsr} of the cloud, which is adopted from the N_2H^+ peak velocity. The spatial positions of the profiles are shown with filled white boxes in the 250 μm *Herschel* image (upper right corner) from 1–30, starting from extreme south toward the west along the filament. The protostar L1157-mm and clump C2 are marked by black and white arrows, respectively. The integrated intensity contours of $C^{18}O$ (1–0) shown in red are obtained by summing the flux over velocity intervals from 2.2–3.0 km s^{-1}. The contours start from 6σ with intervals of 4σ, where $\sigma \sim 0.019$ K km s^{-1}. The cyan contours show the blueshifted (toward the north) and redshifted lobe (towards the south) of the bipolar outflow. The levels for the blueshifted lobe range from 0.12–0.5 in steps of 0.08 K km s^{-1}, and for the redshifted lobe, they are in range of 3.9–6.9 K km s^{-1} in intervals of 1 K km s^{-1}. The ^{12}CO line was integrated from −2.2 to +2.3 km s^{-1} for the high-velocity wings in the southern lobe and from 3.0 to 3.9 km s^{-1} in the northern lobe.

was detected. The variation in the centroid velocity (V_{lsr}) all along the spine of the filament is shown in Fig. 8(c). The peak velocity changes from 2.64 to 2.78 km s^{-1} (2–3 velocity channels). The filament appears to be velocity coherent because there is no significant change in the peak velocity. This is consistent with previous studies of nearby filaments forming low-mass stars (Hacar & Tafalla 2011). The mean dispersion in the centroid velocities obtained from the Gaussian fit is found to be ∼0.03 km s^{-1} . To the west of the C1, the east-west segment of the filament shows an almost constant value of V_{lsr} (∼2.7 km s^{-1}). Compared to this, the velocity structure of the north-south branch shows discernible variation. No notable variation in the values of V_{lsr} obtained from $C^{18}O$ lines is seen along the filament, except at the position where the north-west segment of the filament changes direction toward the east-west segment.

The N_2H^+ (1–0) line emission was detected toward both C1 and C2, with emission being prominent in regions around C1. The seven components in the N_2H^+ (1–0) spectra were simultaneously fit with seven Gaussian forms, with the line parameters given by Caselli et al. (1995). We obtained V_{lsr} of the cloud, line width, and total optical depth of all the components using the fitting results. The peak velocity in the N_2H^+ lines varies from 2.54–2.74 km s^{-1}. The peak velocities obtained from the N_2H^+ line toward C1 and C2 along the filament spine are shown in Fig. 8(c). The V_{lsr} of C1 and C2 was estimated as 2.62 km s^{-1} and for 2.72 km s^{-1} , respectively. The N_2H^+ line shows a systematic change in the velocity at the position of L1157-mm. The velocity gradient estimated using the N_2H^+ emission is found to be 0.37 km s^{-1} pc^{-1}. Chiang et al. (2012) detected N_2H^+ emission across an elongated region of ∼30 000 au (considering a distance of 340 pc), which is consistent with the flattened structure seen by Looney et al. (2007). Systematic variations in the velocity are seen in the N_2H^+ emission across the flattened envelope at ∼30 000 au (Chiang et al. 2012), similar to the variations noted by us at ∼0.1 pc scale. This suggests that the variations in the velocity observed at different scales (Chiang et al. 2012; Kwon et al. 2015) are most likely inherited from the bulk motion of the gas at the cloud scale.

The line width of a spectral line is a combination of thermal and nonthermal motions (Myers 1983). Nonthermal motions generally arise from turbulence in a cloud or core-scale mechanisms. We separated out the thermal component from the observed line width obtained from the Gaussian fitting analysis with the assumption that the two components are independent of each other. The nonthermal component is calculated as,

$$\sigma_{nt} = \sqrt{(\sigma^{obs})^2 - (\sigma^{th})^2} \quad (9)$$

where σ^{th} is $\sqrt{kT/\mu m_{obs}}$, thermal velocity dispersion, μ is the molecular weight of the observed $C^{18}O$ molecule, T is the gas temperature, and k is the Boltzmann constant. The Mach number (M) is defined as the ratio of the nonthermal component (σ_{nt}) and isothermal sound speed (c_s) shown in panel (d) of Fig. 8. The variation shows the extent of nonthermal motions distributed along the positions of the filament. We find that much of the gas in the filament is subsonic as $M \leq 1$. Only the region

around the protostar shows the signature of turbulent motions as $\sigma_{nt} \geq c_s$. The $C^{18}O$ peak line temperature is plotted as a function of position in panel (e) of Fig. 8. The intensity peak observed in $C^{18}O$ toward C1 is found to be shifted from the peak intensity in dust emission. The reason for this might be the depletion of the $C^{18}O$ molecules from the gas phase in the high-density regions. On the other hand, the $C^{18}O$ line intensity peaks in the vicinity of C2 ($T_{mb} \sim 3.0$ K) and remains roughly constant at T_{mb} of 1.0−3.0 K throughout the parts of the filament. The $C^{18}O$ emission is lower at the position of C1, where dust emission is brightest and $C^{18}O$ is comparable to other positions along the east-west branch. In contrast to this, $C^{18}O$ emission is strongest at the position of C2, where dust emission is second brightest. $C^{18}O$ might be highly depleted or photodissociated in the region around C1. However, clump C2 appears to be less strongly depleted than core C1. This suggests that C2 is a chemically younger core than C1. Overall, L1157 is velocity-coherent and mostly subsonic throughout its length, but there is internal dynamics around cores C1 and C2.

We derived the total mass of the cloud by summing all the $N(H_2)$ values falling within the half-maximum contour level in the intensity map of $C^{18}O$ as shown in Fig. 9, where it covers the high-density region of the cloud. The corresponding pixels in the dust column density map were used to calculate the mass of the cloud by dust emission. The mass of the L1157 cloud based on the gas emission was estimated as ∼8 $M_\odot$, whereas the mass of the cloud by dust emission was calculated as 16 $M_\odot$. There is a difference by a factor of more than 2 between the mass ($M(H_2)$) calculated from $C^{18}O$ observations and the *Herschel* dust emission map. We expect the coupling of gas and dust in the ISM at volume densities of $\sim 10^5$ cm^{-3}, which do not correspond to the critical density of $C^{18}O$ molecules (Goldsmith 2001). The typical uncertainty in estimating the $M(H_2)$ value using dust emission is a factor of 2. The dominant factor contributing to the error in the mass estimation is the uncertainty in the opacity law. This value is an upper limit because we lack information on the inclination of the filament. The difference between the $M(H_2)$ values derived from gas and dust can be attributed to various factors. The $C^{18}O$ molecules can deplete and freeze out onto dust grains in high-density regions ($n_{H_2} \geq 10^5$ cm^{-3}) and low temperatures ($T \leq 20$ K). In addition, *Herschel* is capable of tracing the dust column, where the temperatures are higher, but the $C^{18}O$ line might be affected by the interstellar radiation field (ISRF) and become photodissociated at less dense regions of the cloud (e.g., Caselli et al. 1999; Tafalla et al. 2004; Spezzano et al. 2016). The gas column density can change as a result of variation in CO-to-H_2 conversion factor or abundance ratio of optically thick ^{12}CO and optically thin $C^{18}O$ tracers according to metallicity and column density gradients (Pineda et al. 2010; Bolatto et al. 2013).

4.6. Physical parameters of clump C2

Clump C1, which is currently forming the protostar L1157-mm, shows supersonic turbulent motions in the $C^{18}O$ lines. The dust temperature was found to be ∼15 K. Previous studies have characterized C1 using dust continuum and line-mapping observations at different spatial and spectral resolutions (Gueth et al. 1997). In this section we determine the properties of C2 to characterize its evolutionary state. Clump C2 has a peak dust temperature (T_d) ∼12 K and peak column density $\sim 9 \times 10^{21}$ cm^{-2}. As discussed earlier, there exists a blue-red asymmetry in ^{12}CO lines towards the center of C2, and $C^{18}O$ peaks at the velocity of the self-absorption, indicating an inward motion (Figs. 9 and 10). The lack of high-velocity wings in the line profile suggests that

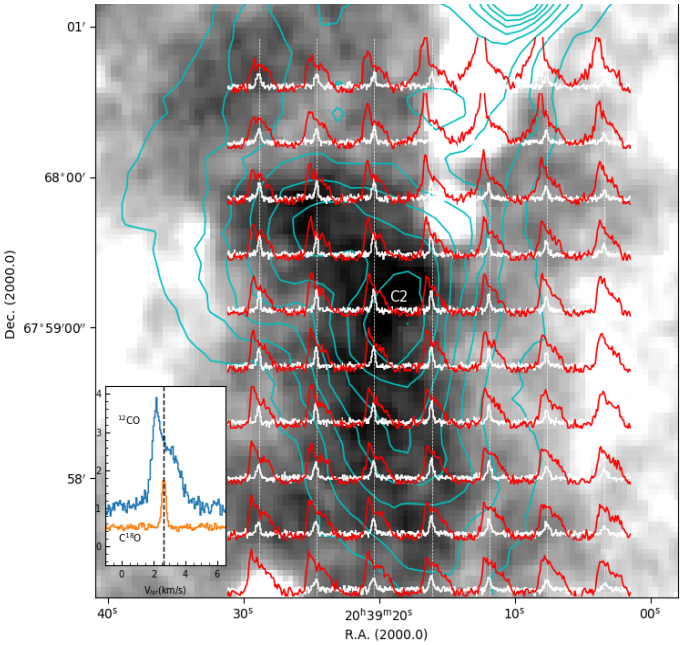

Fig. 10. ^{12}CO (red) and $C^{18}O$ (white) profiles overlaid on the 12 μm WISE emission map; C2 is marked. The cyan contours show the 250 μm dust intensity emission, and the contour levels are in the range 50–120 MJy sr^{-1} in steps of 10 MJy sr^{-1}. In the inset we show two profiles for the ^{12}CO (blue) and $C^{18}O$ lines (orange) averaged over the half-maximum contour in the intensity map of the N_2H^+ line.

the region is not affected by the outflow, although the southern edge of the blueshifted lobe of the outflow spatially coincides with the outer periphery of C2. The outflow is almost in the plane of sky with an inclination angle of 10° (Gueth et al. 1996). We quantified the outflow energetics with its mass and kinetic energy as 0.05 $M_\odot$ and 1.2×10^{43} ergs, respectively. The sources of uncertainty in estimating the outflow parameters depend on the velocity boundary between the high-velocity wings and the ambient velocity and the inclination angle with respect to the line of sight. The gravitationally binding energy of C2 is calculated as 0.53×10^{43} ergs. Thus, the outflow has the potential to disturb the ambient gas and may affect C2 in the future. The motion of the gas molecules around C2 is very quiescent, with subsonic turbulence and high $C^{18}O$ intensity. Figure 8c shows that the subsonic nonthermal motions are mostly associated with the region around C2. The properties of prestellar or starless cores in low-mass star-forming regions such as Taurus and Ophiuchus have been studied in detail (di Francesco et al. 2007; Gregersen & II 2000; Onishi et al. 2002; Motte et al. 1998), and the values found here for C2 are consistent with the typical properties of a starless core.

The measure of nonthermal line widths using molecular line diagnostics can be used to investigate whether the core is virially bound. We derived the virial mass of C2 using the averaged total velocity dispersion of the $C^{18}O$ line. If the mass of the clump is less than the virial mass, the cloud is not gravitationally bound and may expand. We derived the virial mass using the formula (MacLaren et al. 1988),

$$M_{vir} = \frac{k\sigma^2 R}{G}, \tag{10}$$

where k depends on the density distribution, G is the gravitational constant, and R is the cloud radius. The total velocity

dispersion is given by the equation

$$\sigma = \sqrt{\frac{kT_{\rm kin}}{\mu_{m_{\rm H}}} + \sigma_{\rm nt}^2} \quad (11)$$

Assuming a Gaussian velocity distribution and density profile distribution as $\rho = r^{-2}$, we can also express this equation in terms of solar mass as $M_{\rm virial} = 126\Delta v^2 R$, where Δv is the FWHM velocity of the $C^{18}O$ lines in km s^{-1} along the line of sight, and R is the radius in parsec units. By approximating C2 as an ellipse on the sky projection, the radius of the core was estimated as $\sqrt{FWHMx} \times \sqrt{FWHMy}$, where FWHM$x$ and FWHMy are the FWHM diameters along the major and minor axis, respectively. The value of the average FWHM velocity of the gas was calculated to be 0.5 km s^{-1}. We calculated the effective radius of C2 as ∼0.1 pc using the FWHM of the major axis ∼1.3′ and of the minor axis ∼0.7′. The virial mass of C2 was estimated to be ∼3.1 $M_\odot$. The main contribution to the uncertainty in the calculation of the virial mass comes from the uncertainty in the distance estimate, which is ∼1%. The variation of 5% in the value of virial mass is due to the distance uncertainty. We summed all the pixels whose column density values fell within the derived radius of clump C2 in a moment-zero map of the $C^{18}O$ line. The total gas mass of C2 is calculated to be $\sim 2.5 \pm 0.3\ M_\odot$. We found that clump C2 is on the verge of being gravitationally bound because $M_{\rm virial} \sim M_{\rm gas}$. The dust mass around clump C2 is calculated to be ∼5 $M_\odot$ using the same region as in the calculation of the gas mass.

The N_2H^+ line traces the dynamics of the dense central part of the core, and the $C^{18}O$ line traces the dynamics of the surrounding less dense material in the envelope. We studied the core-to-envelope motion around C1 and C2 by comparing the centroid velocity of the N_2H^+ and $C^{18}O$ lines and the velocity dispersion. The velocities of the different tracers match, as we also show in Fig. 8. The average difference in centroid velocities of $C^{18}O$ and N_2H^+ around clump C2 is 0.03 ± 0.02 km s^{-1} and around core C1, it is 0.06 ± 0.02 km s^{-1}, which means that the velocities of the different tracers differ on average by less than one-fifth or one-third of the sound speed. This good match rules out any significant relative motions between different density regimes of the gas, and in particular, it rules out the possibility of any systematic drift between the dense cores (traced by N_2H^+) and the surrounding gas (traced by $C^{18}O$). This result agrees well with previous studies that probed the relative motion between the dense inner region and the envelope of the cores (Kirk et al. 2007; Walsh et al. 2004; Ayliffe et al. 2007). The line width obtained for the $C^{18}O$ line is found to be relatively broader (by one to two channels around core C1) than that of N_2H^+ (1–0), as shown in Fig. 11. The difference in line width around core C1 is within a channel spacing for the two tracers. The motions in C2 are subsonic in the $C^{18}O$ and N_2H^+ lines compared to the motion of C1. This line broadening is consistent with previous studies, where starless cores were expected to have less turbulent motions and protostellar cores show a broader line width (Kirk et al. 2007).

The N_2H^+ and $C^{18}O$ lines can be used to determine the extent of the chemical evolution of the dense cores. N_2H^+ can only form in a significant amount after $C^{18}O$ freezes out onto dust grains because both the molecules form by competing reactions (Caselli et al. 1999). N_2H^+ is observed to be good tracer of gas at densities $\sim 10^5$–10^6 cm^{-3}, whereas $C^{18}O$ is depleted at these densities (Tafalla et al. 2002). At later stages of the evolution, when the central protostar formation has taken place, the

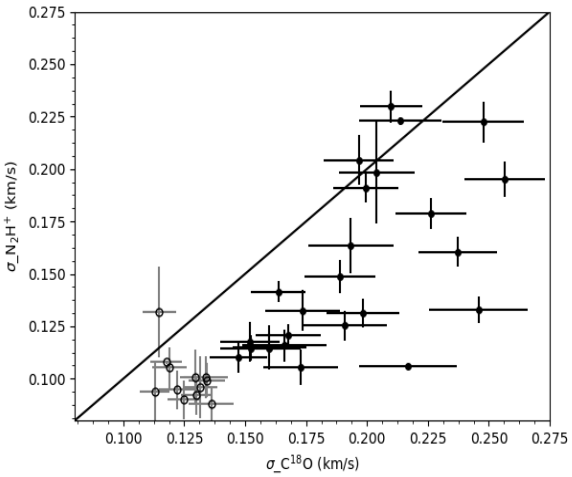

Fig. 11. Variation of the velocity dispersion measured in the $C^{18}O$ and N_2H^+ profiles. The filled circles are the points near C1, and unfilled circles are the points around C2.

N_2H^+ is destroyed by the rise in temperature, and CO molecules start to form. We used the integrated intensity of the $C^{18}O$ and N_2H^+ lines to calculate the intensity ratio. If this ratio is higher than one, it implies that the core has not evolved to the extent that the carbon molecules could freeze out onto the surface of dust grains, and therefore the core is chemically young. We averaged the intensity values around the starless core C2 where significant ($\geq 3\sigma$) emission of N_2H^+ is obtained. The ratio is found to be greater than one, which implies that the core has not yet evolved chemically. Core C1 shows a highly enhanced distribution of the N_2H^+ line. This may be due to the significant depletion or photodissociation of $C^{18}O$ molecules in the core. These molecules usually play a role for the destruction of N_2H^+ (Caselli et al. 1999). N_2H^+ in C2 core is also enhanced, but not as much as C1 core. This can also be explained by an overabundance of $C^{18}O$ molecules compared to C1 core.

4.7. Motion of the L1147/1158 and L1172/1174 complexes

A PanSTARRs z-band ($\lambda_{\rm eff}$ = 8668.5 Å) image (Chambers et al. 2016) of the field containing L1157 (the contrast of the original image is adjusted to highlight the features) in the Galactic coordinate system is shown in Fig. 12. The shape of the southern boundary of the east-west segment is found to be sinuous. Odenwald & Rickard (1987) and Odenwald (1988) have cataloged a number of high-latitude cometary or filamentary objects gleaned from IRAS images and suggested that their morphologies might be a result of cloud-ISM interaction. A flow of velocity of V around an object of length L can be characterized using the Reynolds number ($R_{\rm e} = \rho LV/\mu$), where ρ is the ambient fluid density, and μ is the fluid viscosity. While flows of extremely low (∼10) and intermediate (∼50) values of $R_{\rm e}$ are expected to show a smooth laminar flow pattern and irregular structures and vortices, respectively, higher values of $R_{\rm e}(\gg 100)$ are expected to produce a fully turbulent flow. Odenwald (1988) suggested that for a relatively low value of $R_{\rm e}$ ($\lesssim 10$), the mass lost by ablation through the motion of a cloud through ambient medium can form long sinuous filaments.

To calculate the space velocity of the L1147/1158 complex, which is required to estimate the value of $R_{\rm e}$, we made use of the proper motion values of the YSOs associated with the region and the radial velocities of the clouds. Because the L1147/1158

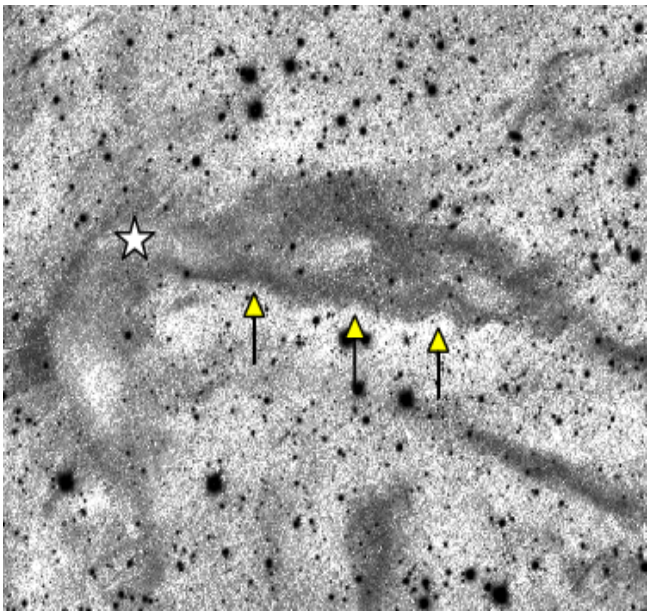

Fig. 12. PanSTARRs z-band image of the field containing L1157. The sinuous features are identified with arrows and the position of the protostar L1157-IRS is identified using a star. The contrast of the original image is adjusted to reveal the features.

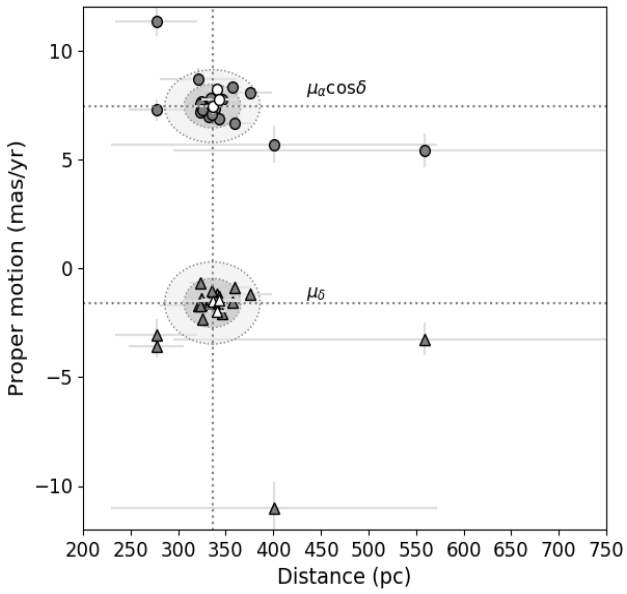

Fig. 13. Proper motion values and distances of the 23 YSO candidates associated with the L1147/1158 and L1172/1174 complexes. The darker and lighter shaded ellipses are drawn using three and five times the median absolute deviation values of the distance and the proper motions, respectively.

($l \sim 102.2°$, $b \sim +15.3°$) and L1172/1174 ($l \sim 104.03°$, $b \sim +14.3°$) complexes are located close to each other (~2°) in projection and share similar radial velocities (Myers et al. 1983; Yonekura et al. 1997), we also included the YSOs associated with L1172/1174 in our analysis. A total of 58 YSO candidates are identified so far in the vicinity of L1172/1174 (Kun et al. 2009; Kirk et al. 2009; Yuan et al. 2013). We found *Gaia* DR2 counterparts for 20 of them well within a search radius of 1″. As in the case of L1147/1158, we obtained their distances from the Bailer-Jones et al. (2018) catalog and $\mu_{\alpha\star}$ and μ_δ values from the Gaia Collaboration (2018) catalog. Again, we considered only sources whose parallax and proper motion values are greater than or equal to three times the corresponding errors. The *Gaia* DR2 results are presented in Table 2 and shown in Fig. 13. Of the 20 sources in the L1172/1174 complex, 15 are clustered, as are 3 sources in the L1147/1158 complex. The median (median absolute deviation) values of the distance $\mu_{\alpha\star}$ and μ_δ for sources in the L1172/1174 complex are 335 (11) pc, 7.301 (0.386) mas yr^{-1} and −1.619 (0.427) mas yr^{-1}, respectively. The previous distance estimate to L1172/1174 was 288 ± 25 pc (Straizys et al. 1992). When the YSO candidates from the two complexes are combined, we obtain median (median absolute deviation) values of the distance $\mu_{\alpha\star}$ and μ_δ of 336 (10) pc, 7.436 (0.334) and −1.599 (0.377) mas yr^{-1}, respectively.

The darker shaded ellipses in Fig. 13 are drawn using three times the median absolute deviation values of the distance and proper motion. All the 3 and the 12 YSOs associated with L1147/1158 and L1172/1174, respectively, are found within the distance-$\mu_{\alpha\star}$ ellipse. Four more YSOs associated with L1172/1174 could be included if we were to consider the ellipses drawn with five times the median absolute deviation values of the distance and $\mu_{\alpha\star}$. Similarly, all the 3 and the 14 YSOs associated with L1147/1158 and L1172/1174, respectively, are found within the distance-μ_δ ellipse. Two more from L1172/1174 are added if we were to consider the ellipses drawn with five times the median absolute deviation values of the distance and μ_δ. Four sources are found to be clear outliers. The lighter shaded ellipses in Fig. 13 are drawn using five times the median absolute deviation values of distance and proper motion. All the sources found within these ellipses are considered part of the L1147/1158 and L1172/1174 complexes and were included in our analysis. The results imply that the two complexes are related to each other both spatially and kinematically.

The proper motions of the sources measured by the *Gaia* are in the equatorial system of coordinates. To understand the motion of objects in the Galaxy, we need to transform the proper motion values from the equatorial to the Galactic coordinate system $\mu_{l\star} = \mu_l \cos b$ and μ_b. We transformed the proper motion values using the expression (Poleski 2013)

$$\begin{bmatrix} \mu_{l\star} \\ \mu_b \end{bmatrix} = \frac{1}{\cos b} \begin{bmatrix} C_1 & C_2 \\ -C_2 & C_1 \end{bmatrix} \begin{bmatrix} \mu_{\alpha\star} \\ \mu_\delta \end{bmatrix}, \tag{12}$$

where the term $\cos b = \sqrt{C_1^2 + C_2^2}$ and the coefficients C_1 and C_2 are given as

$$\begin{aligned} C_1 &= \sin\delta_G \cos\delta - \cos\delta_G \sin\delta \cos(\alpha - \alpha_G) \\ C_2 &= \cos\delta_G \sin(\alpha - \alpha_G). \end{aligned} \tag{13}$$

The equatorial coordinates (α_G, δ_G) of the north Galactic pole are taken to be 192°.85948 and 27°.12825, respectively (Poleski 2013). The proper motion of the YSO candidates in the Galactic coordinates are drawn in Fig. 14. The mean values of $\mu_{l\star}$ and μ_b are found to be 3.499 and −6.815 mas yr^{-1}, respectively, and the corresponding proper motion position angle is found to be 153°. The arrows show the sense of the motion of the sources on the sky plane. If we assume that the cloud and the YSO candidates are expected to share similar kinematics as a result of being born inside the cloud, then the arrows should also represent the motion of the clouds on the sky plane. The reflection nebulosity around a number of these YSO candidates provides evidence that they are clearly associated with the cloud.

Based on our N_2H^+ observations, the V_{lsr} velocity of L1157 is found to be +2.65 km s^{-1}. Yonekura et al. (1997) carried out

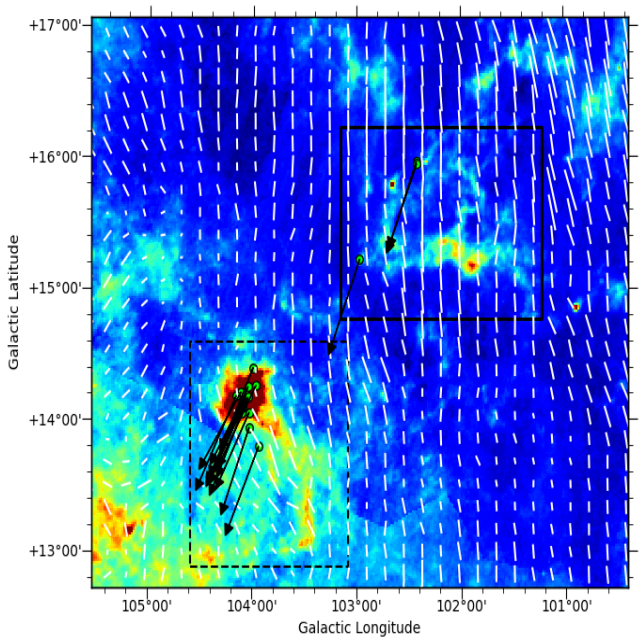

Fig. 14. *Planck* polarization vectors in white overplotted over the color scale *AKARI* 160 μm emission map of the L1147/L1158 complex. Proper motion values and distances of 19 YSO candidates associated with the L1147/1158 and L1172/1174 complexes. The box in bold lines shows the L1147/1158 complex, and the dashed lines show the L1172/1174 complex.

a molecular line survey in the direction of the Cepheus region that included the L1148/L1157 and L1172/1174 cloud complexes. They found nine clouds that showed the $V_{\rm lsr}$ velocity in the range of +2.6 km s^{-1} to +4.8 km s^{-1}. The mean value of the $V_{\rm lsr}$ velocities of these nine clouds is found to be ∼3.0 km s^{-1}. We took this value as the radial velocity of the two complexes. We converted this value from the LSR system into the heliocentric system as $V_{\rm r} = -10.75$ km s^{-1}. The two tangential velocity components along the Galactic longitude and latitude were calculated using $V_l = 4.74d \times \mu_{l\star}$ and $V_{\rm b} = 4.74d \times \mu_b$, respectively. The factor 4.74 is the ratio of the au expressed in kilometers and the number of seconds in a tropical year. d is the distance in parsec of the individual stars obtained from the Bailer-Jones et al. (2018) catalog. Then we calculated the velocities U, V, and W directed along the rectangular Galactic coordinate axes using the expressions (e.g., Bobylev & Bajkova 2019)

$$\begin{bmatrix} U \\ V \\ W \end{bmatrix} = \begin{bmatrix} \cos l \cos b & -\sin l & -\cos l \sin b \\ \sin l \cos b & \cos l & -\sin l \sin b \\ \sin b & 0 & \cos b \end{bmatrix} \begin{bmatrix} V_{\rm r} \\ V_{\rm l} \\ V_{\rm b} \end{bmatrix}. \quad (14)$$

The velocity U is directed from the Sun toward the Galactic center with the positive direction being toward the Galactic center, V is positive in the direction of Galactic rotation, and W is positive directed to the north Galactic pole. The mean values of (U, V, W) for the 19 YSO candidates toward L1147/L1158 and L1172/1174 cloud complexes are (−3.6, −8.8, −13.3) km s^{-1} with a standard deviation of (0.6, 0.3, 0.9) km s^{-1}. To determine the motion of the complexes with respect to the Galactic frame of reference, we transformed the heliocentric velocities to the LSR velocities by subtracting the motion of the Sun with respect to the LSR from the heliocentric velocities. In a number of studies (e.g., Trick et al. 2019; López-Corredoira & Sylos Labini 2019) the velocity components of the motion of the Sun with respect to the LSR estimated by Schönrich et al. (2010) of (U, V, W)$_\odot$ = ($11.1^{+0.69}_{-0.75}$, $12.24^{+0.47}_{-0.47}$, $7.25^{+0.37}_{-0.36}$) km s^{-1} are used. However, based on the *Gaia* DR2 data, the velocity components of the Sun's motion have recently been reevaluated using, for example, stars (Li et al. 2019; Ding et al. 2019), open star clusters (Bobylev & Bajkova 2019), OB star samples (Bobylev & Bajkova 2018), and white dwarfs (Rowell & Kilic 2019). We used the most recent values of (U, V, W)$_\odot$ = (7.88, 11.17, 8.28) ± (0.48, 0.63, 0.45) km s^{-1} obtained by Bobylev & Bajkova (2019) for the transformation from the heliocentric to the LSR velocities. The mean value of (u, v, w) estimated for the 19 YSO candidates toward the L1148/L1157 and L1172/1174 cloud complexes is found to be (4.3, −2.9, −5.0) km s^{-1} with a standard deviation of (0.6, 0.3, 0.9) km s^{-1}. The results imply that the L1148/L1157 and L1172/1174 cloud complexes collectively move in the direction of the Galactic center, opposite to the Galactic rotation, and approach the Galactic plane.

The motion of the complex is presented on a rectangular (x, y, z) coordinate system with the Sun as the origin, as shown in Fig. 15. The Ox -axis runs parallel to the Sun-Galactic center direction, Oy in the Galactic plane but perpendicular to the Ox and Oz is perpendicular to the Galactic plane. The positive direction in Ox, Oy, and Oz is the direction toward the Galactic center, in the direction of the Galactic rotation and toward the Galactic north pole, respectively. We computed the position of the complexes (X, Y, Z) as (−80, 319, 85) pc. The resulting velocity of the complexes as a whole is found to be ∼7 km s^{-1}.

The *Planck* magnetic field vectors from a region containing the two complexes are also shown in Fig. 14. Although there are regions where the projected magnetic fields show a rotation in the position angles (toward the L1172/1174 complex), as a whole, the projected field orientation toward the region is found to be almost parallel to the Galactic latitude. The projected magnetic field direction obtained from the median value of the Galactic polarization position angles is ∼5° from the north. This implies that the projected motion of the complexes creates an angle of 32° with respect to the projected magnetic field orientation. Following the procedure from Odenwald & Rickard (1987) and Odenwald (1988), we made a rough estimate of the value of R$_e$ for L1157 and found it to be ∼3. The main contribution to the uncertainty in the calculation of $R_{\rm e}$ comes from the large uncertainty in the estimation of the density and the viscosity of the ambient medium. We ignored the effects of the magnetic field in our calculation because the offset between the projected magnetic field and the direction of the cloud motion is ∼30°. Studies with various values of offsets between the orientation of the magnetic field lines and the direction of the cloud motion have shown that only for large enough offsets do magnetic fields play a significant role in the dynamical evolution of the cloud (Mac Low et al. 1994; Jones et al. 1996; Miniati et al. 1999). The number density of the ambient medium is estimated to be 0.09 cm^{-3} by adopting a density of 0.17 cm^{-3} along the Galactic plane and an exponential scale height of 125 pc (Odenwald 1988). Assuming that the cloud is in pressure equilibrium with the ambient medium, we estimated the temperature of the ambient medium to be ∼10^6 K using the average values of the number density and temperature of the cloud calculated from the dust emission. We used V = 7 km s^{-1} and L = 1 pc in the calculation. The low value of $R_{\rm e}$ is consistent with the smooth morphology of the cloud structure, as depicted in Fig. 12.

Several shell structures, such as the Cepheus flare shell (CFS), which is an old supernova remnant, and Loop III, which is a giant radio continuum feature (Kirk et al. 2009), are taken as signature of multiple supernova explosions that might have occurred toward the region. The complexes L1147/1158 and

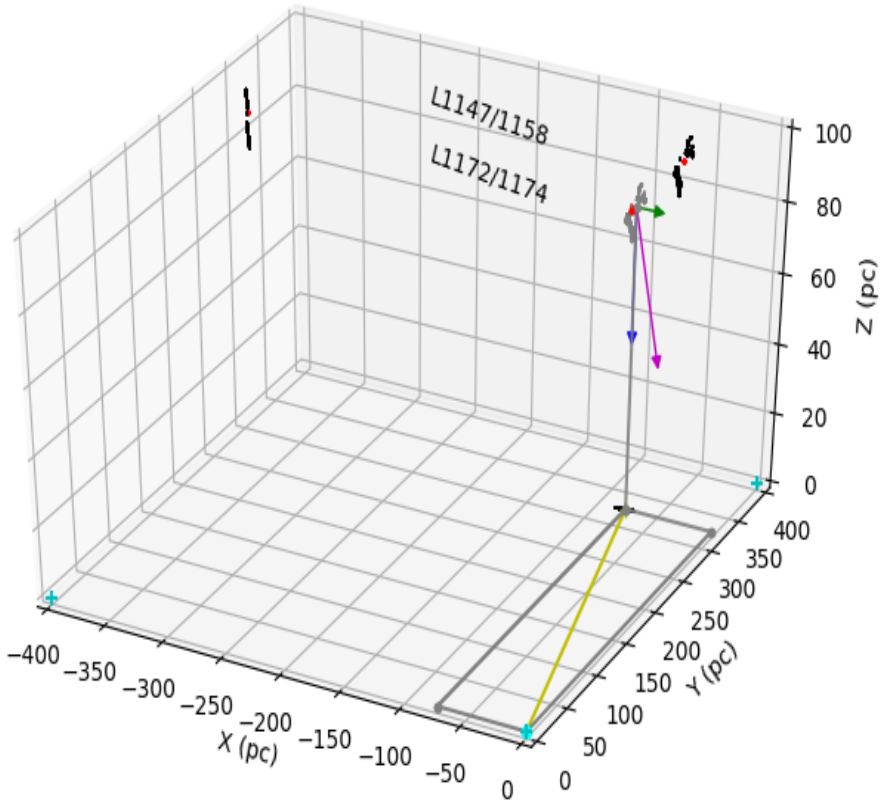

Fig. 15. 3D motion of the L1147/1158 and L1172/1174 complexes in a rectangular coordinate system with the Sun as the origin. The *X*-, *Y*-, and *Z*-axes run parallel to the Sun-Galactic center vector, perpendicular to the Sun-Galactic center vector, and perpendicular to the Galactic plane, respectively. The positive direction of the *X*-, *Y*-, and *Z*-axes is the direction toward the Galactic center, in the direction of Galactic rotation, and toward the Galactic north pole, respectively. The green, red, and blue arrows represent the velocity components in the *X*-, *Y*-, and *Z*-axes, respectively. The magenta arrow represents the resulting velocity of the complex. The yellow line shows the projection of the distance of the complex on the Galactic plane. The scale of the vectors is taken as eight times the magnitude of the velocity.

L1172/1174 are located outside the CFS but at the periphery of Loop III (Kirk et al. 2009). It is possible that these supernova events may have transferred the material toward the high-latitude regions and that the material now moves downward toward the Galactic plane. Harjunpaa et al. (1991) studied the entire L1147/1158 complex and noted that the southeastern boundary of the complex shows a remarkably sharp edge parallel to the Galactic plane. Based on the spectra obtained along the latitude, $l = 102°.73$, they detected a velocity gradient and attributed it to cloud rotation with the angular velocity vector pointing perpendicular to the Galactic plane. Alternatively, the sharp boundary and the velocity gradient might be due to the bulk motion of the cloud material. The star formation in the clouds associated with the complexes might be a result of their interaction with the ambient medium as they travel.

5. Conclusions

We presented results of a study conducted on the molecular cloud L1157, which is part of the cloud complex L1147/1158. Currently, a Class 0 protostar, L1157-mm, with a spectacular bipolar outflow is being formed. The extreme youth of the protostar implies that the initial conditions that guided the cloud to form a star may still be preserved. We made *R*-band polarimetry of the cloud to trace the magnetic field geometry of the cloud. We also made observations in the ^{12}CO, C^{18}O, and N_2H^+ ($J = 1-0$) lines to investigate the kinematics of the material associated with the cloud. The main results are summarized below.

1. We estimated the distance to the L1147/1158 complex using the YSOs associated with the cloud complex. The distances of the YSOs were estimated based on the parallax measurements and the proper motion values obtained from the *Gaia* DR2 database. The estimated distance is 340 ± 3 pc.
2. We obtained polarization measurements of 62 stars projected toward the direction of L1157 (within a region of $0.3° \times 0.3°$ field). Based on the plot of the degree of polarization versus distance for the stars observed by us and those from the Heiles (2000) catalog, we present additional evidence of the cloud at a distance of ∼340 pc.
3. Using the *Filfinder* algorithm on the dust column density map of L1157 obtained from the *Herschel* data, we traced a filament that is found to be ∼1.2 pc in length and oriented at a PA of 79° (east-west segment). Near to the protostar, the filament changes its orientation and becomes almost perpendicular (north-south segment). Using the *Radfil* algorithm, we estimated the average filament width to be ∼0.09 pc, and the radial distribution of the material was fit with a Plummer-like density profile with a power-law index of $p = 3$. Using the *Clumpfind* algorithm, we identified two cores (C1 and C2) that are found to be located in the filament. In one of these cores, L1157-mm is currently embedded.
4. The ICMF traced by our *R*-band polarization measurements of the stellar background to the cloud is found to be well ordered at a ∼0.2−2 pc scale. The geometry of the ICMF inferred from the *Planck* 353 GHz data was found to agree well with our *R*-band polarization results. The strength of the magnetic field calculated based on our data is found to be ∼50 μG. The ICMF is oriented at a PA of 127° ± 12°.
5. Based on the relative orientations between the ISMF, CMF, filament, outflow, and the hourglass morphology of the magnetic field at the core scale with its symmetry axis orthogonal to the major axis of the flattened pseudo-disk, we suggest that the magnetic field has played an important role in the evolution of L1157 to becoming a star-forming core.
6. We made ^{12}CO, C^{18}O, and N_2H^+ line observations of the entire region covering the L1157 cloud. C^{18}O is detected at points throughout the ∼1.2 pc long filament and is found to correlate well with the dust emission. A blue-red asymmetry is observed in ^{12}CO toward both C1 and C2, with C^{18}O peaking at the systematic velocity of the cloud. This signifies

infall motion of the material. We found no significant change in the V_{lsr} velocity along the filament, except at the location where the north-south segment changes its direction toward the east-west segment of the filament. The N_2H^+ ($J = 1-0$) line also shows a systematic change in the velocity across C1 that is suggestive of a bulk motion in the gas.

7. The east-west segment of the filament presents a sinuous structure. It is believed that the sinuous features seen in clouds occur due to cloud-ISM interaction. The dynamical state of such interactions depends on the Reynolds number, which is found to be ~3 in L1157. For such a low value ($\lesssim$10) of Reynolds number, the cloud motion through the ambient medium can cause mass loss by ablation and can form long sinuous filaments.

Acknowledgements. This work has made use of data from the European Space Agency (ESA) mission *Gaia* (https://www.cosmos.esa.int/gaia), processed by the *Gaia* Data Processing and Analysis Consortium (DPAC, https://www.cosmos.esa.int/web/gaia/dpac/consortium). Funding for the DPAC has been provided by national institutions, in particular the institutions participating in the *Gaia* Multilateral Agreement. The *Planck* Legacy Archive (PLA) contains all public products originating from the *Planck* mission, and we take the opportunity to thank ESA/*Planck* and the Planck Collaboration for the same. C.W.L. is supported by Basic Science Research Program through the National Research Foundation of Korea (NRF) funded by the Ministry of Education, Science and Technology (NRF-2019R1A2C1010851). A.S. acknowledges financial support from the NSF through grant AST-1715876. This research has made use of the SIMBAD database, operated at CDS, Strasbourg, France. We also used data provided by the SkyView which is developed with generous support from the NASA AISR and ADP programs (PI: Thomas A. McGlynn) under the auspices of the High Energy Astrophysics Science Archive Research Center (HEASARC) at the NASA/ GSFC Astrophysics Science Division.

References

Allen, A., Shu, F. H., & Li, Z.-Y. 2003a, ApJ, 599, 351
Allen, A., Li, Z.-Y., & Shu, F. H. 2003b, ApJ, 599, 363
Alves, F. O., & Franco, G. A. P. 2007, A&A, 470, 597
Alves, F. O., Franco, G. A. P., & Girart, J. M. 2008, A&A, 486, L13
Andre, P. 1996, Mem. Soc. Astron. It., 67, 901
Andre, P., Ward-Thompson, D., & Barsony, M. 1993, ApJ, 406, 122
André, P., Men'shchikov, A., Bontemps, S., et al. 2010, A&A, 518, L102
André, P., Di Francesco, J., Ward-Thompson, D., et al. 2014, Protostars and Planets VI (Tucson: University of Arizona Press), 27
Aniano, G., Draine, B. T., Gordon, K. D., & Sandstrom, K. 2011, PASP, 123, 1218
Arce, H. G., Santiago-García, J., Jørgensen, J. K., Tafalla, M., & Bachiller, R. 2008, ApJ, 681, L21
Arnal, E. M., Morras, R., & Rizzo, J. R. 1993, MNRAS, 265, 1
Arzoumanian, D., André, P., Didelon, P., et al. 2011, A&A, 529, L6
Arzoumanian, D., André, P., Könyves, V., et al. 2019, A&A, 621, A42
Audit, E., & Hennebelle, P. 2005, A&A, 433, 1
Avery, L. W., & Chiao, M. 1996, ApJ, 463, 642
Ayliffe, B. A., Langdon, J. C., Cohl, H. S., & Bate, M. R. 2007, MNRAS, 374, 1198
Bachiller, R., Pérez Gutiérrez, M., Kumar, M. S. N., & Tafalla, M. 2001, A&A, 372, 899
Bailer-Jones, C. A. L., Rybizki, J., Fouesneau, M., Mantelet, G., & Andrae, R. 2018, AJ, 156, 58
Ballesteros-Paredes, J., Hartmann, L., & Vázquez-Semadeni, E. 1999, ApJ, 527, 285
Balsara, D., Ward-Thompson, D., & Crutcher, R. M. 2001, MNRAS, 327, 715
Banerjee, R., Pudritz, R. E., & Anderson, D. W. 2006, MNRAS, 373, 1091
Benson, P. J., Ladd, E. F., Myers, P. C., Campbell, B. G., & Walmsley, C. M. 1988, BAAS, 20, 693
Bergin, E. A., & Tafalla, M. 2007, ARA&A, 45, 339
Bergin, E. A., Alves, J., Huard, T., & Lada, C. J. 2002, ApJ, 570, L101
Bobylev, V. V., & Bajkova, A. T. 2018, Astron. Lett., 44, 676
Bobylev, V. V., & Bajkova, A. T. 2019, Astron. Lett., 45, 109
Bolatto, A. D., Wolfire, M., & Leroy, A. K. 2013, ARA&A, 51, 207
Caselli, P., Myers, P. C., & Thaddeus, P. 1995, ApJ, 455, L77
Caselli, P., Walmsley, C. M., Tafalla, M., Dore, L., & Myers, P. C. 1999, ApJ, 523, L165
Cazaux, S., Martín-Doménech, R., Chen, Y. J., Muñoz Caro, G. M., & González Díaz, C. 2017, ApJ, 849, 80
Cernis, K. 1987, Ap&SS, 133, 355
Chambers, K. C., Magnier, E. A., Metcalfe, N., et al. 2016, ArXiv e-prints [arXiv:1612.05560]
Chandrasekhar, S., & Fermi, E. 1953, ApJ, 118, 113
Chapman, N. L., Goldsmith, P. F., Pineda, J. L., et al. 2011, ApJ, 741, 21
Chapman, N. L., Davidson, J. A., Goldsmith, P. F., et al. 2013, ApJ, 770, 151
Chiang, H.-F., Looney, L. W., Tobin, J. J., & Hartmann, L. 2010, ApJ, 709, 470
Chiang, H.-F., Looney, L. W., & Tobin, J. J. 2012, ApJ, 756, 168
Clarke, S. D., Whitworth, A. P., Duarte-Cabral, A., & Hubber, D. A. 2017, MNRAS, 468, 2489
Clemens, D. P., El-Batal, A. M., Cerny, C., et al. 2018, ApJ, 867, 79
Crutcher, R. M. 2012, ARA&A, 50, 29
Davis, L. 1951, Phys. Rev., 81, 890
Davis, Jr. L., & Greenstein, J. L. 1951, ApJ, 114, 206
de Avillez, M. A., & Breitschwerdt, D. 2005, A&A, 436, 585
Dickman, R. L. 1978, ApJS, 37, 407
di Francesco, J., Evans, N. J., I., Caselli, P., et al. 2007, in Protostars and Planets V, eds. B. Reipurth, D. Jewitt, & K. Keil (Tucson: University of Arizona Press), 17
Ding, P.-J., Zhu, Z., & Liu, J.-C. 2019, Res. Astron. Astrophys., 19, 068
Dutra, C. M., & Bica, E. 2002, A&A, 383, 631
Fehér, O., Juvela, M., Lunttila, T., et al. 2017, A&A, 606, A102
Fiege, J. D., & Pudritz, R. E. 2000a, ApJ, 534, 291
Fiege, J. D., & Pudritz, R. E. 2000b, MNRAS, 311, 85
Fischera, J., & Martin, P. G. 2012, A&A, 542, A77
Froebrich, D. 2005, ApJS, 156, 169
Gaia Collaboration (Brown, A. G. A., et al.) 2018, A&A, 616, A1
Galli, D., & Shu, F. H. 1993a, ApJ, 417, 220
Galli, D., & Shu, F. H. 1993b, ApJ, 417, 243
Galván-Madrid, R., Liu, H. B., Zhang, Z. Y., et al. 2013, ApJ, 779, 121
Goldsmith, P. F. 2001, ApJ, 557, 736
Gómez, G. C., & Vázquez-Semadeni, E. 2014, ApJ, 791, 124
Gómez, G. C., Vázquez-Semadeni, E., & Zamora-Avilés, M. 2018, MNRAS, 480, 2939
Goodman, A. A. 1995, ASP Conf. Ser., 73, 769
Goodman, A. A., Jones, T. J., Lada, E. A., & Myers, P. C. 1992, ApJ, 399, 108
Goodman, A. A., Jones, T. J., Lada, E. A., & Myers, P. C. 1995, ApJ, 448, 748
Greaves, J. S., Holland, W. S., Minchin, N. R., Murray, A. G., & Stevens, J. A. 1999, A&A, 344, 668
Gregersen, E. M., & Neal, II. J. E. 2000, ApJ, 538, 260
Griffin, M. J., Abergel, A., Abreu, A., et al. 2010, A&A, 518, L3
Gu, Q., & Li, H.-b. 2019, ApJ, 871, L15
Gueth, F., Guilloteau, S., & Bachiller, R. 1996, A&A, 307, 891
Gueth, F., Guilloteau, S., Dutrey, A., & Bachiller, R. 1997, A&A, 323, 943
Guetter, H. H., & Vrba, F. J. 1989, AJ, 98, 611
Hacar, A., & Tafalla, M. 2011, A&A, 533, A34
Harjunpaa, P., Liljestrom, T., & Mattila, K. 1991, A&A, 249, 493
Harjunpää, P., Kaas, A. A., Carlqvist, P., & Gahm, G. F. 1999, A&A, 349, 912
Heiles, C. 2000, AJ, 119, 923
Heitsch, F. 2013, ApJ, 776, 62
Heitsch, F., Hartmann, L. W., & Burkert, A. 2008, ApJ, 683, 786
Heyer, M. H., Vrba, F. J., Snell, R. L., et al. 1987, ApJ, 321, 855
Hildebrand, R. H., Dragovan, M., & Novak, G. 1984, ApJ, 284, L51
Hull, C. L. H., Plambeck, R. L., Bolatto, A. D., et al. 2013, ApJ, 768, 159
Hull, C. L. H., Plambeck, R. L., Kwon, W., et al. 2014, ApJS, 213, 13
Jeong, I.-G., Kang, H., Jung, J., et al. 2019, J. Korean Astron. Soc., 52, 227
Jones, R. V., & Spitzer, Jr., L. 1967, ApJ, 147, 943
Jones, T. W., Ryu, D., & Tregillis, I. L. 1996, ApJ, 473, 365
Kauffmann, J., Bertoldi, F., Bourke, T. L., Evans, II, N. J., & Lee, C. W. 2008, A&A, 487, 993
Kirk, H., Johnstone, D., & Tafalla, M. 2007, ApJ, 668, 1042
Kirk, J. M., Ward-Thompson, D., Di Francesco, J., et al. 2009, ApJS, 185, 198
Kirk, J. M., Ward-Thompson, D., Palmeirim, P., et al. 2013, MNRAS, 432, 1424
Koch, E. W., & Rosolowsky, E. W. 2015, MNRAS, 452, 3435
Könyves, V., André, P., Men'shchikov, A., et al. 2015, A&A, 584, A91
Krumholz, M. R., Crutcher, R. M., & Hull, C. L. H. 2013, ApJ, 767, L11
Kun, M. 1998, ApJS, 115, 59
Kun, M., Balog, Z., Kenyon, S. J., Mamajek, E. E., & Gutermuth, R. A. 2009, ApJS, 185, 451
Kwon, W., Fernández-López, M., Stephens, I. W., & Looney, L. W. 2015, ApJ, 814, 43
Lazarian, A. 1995, ApJ, 453, 229
Lee, C. W., Myers, P. C., & Tafalla, M. 1999, ApJ, 526, 788
Lee, C. W., Myers, P. C., & Tafalla, M. 2001, ApJS, 136, 703
Li, C., Zhao, G., & Yang, C. 2019, ApJ, 872, 205

Li, H.-b., Dowell, C. D., Goodman, A., Hildebrand , R., & Novak, G. 2009, ApJ, 704, 891
Li, H.-B., Yuen, K. H., Otto, F., et al. 2015, Nature, 520, 518
Lindegren, L., Hernández, J., Bombrun, A., et al. 2018, A&A, 616, A2
Liu, H. B., Jiménez-Serra, I., Ho, P. T. P., et al. 2012, ApJ, 756, 10
Loinard, L., Torres, R. M., Mioduszewski, A. J., et al. 2007, ApJ, 671, 546
Looney, L. W., Tobin, J. J., & Kwon, W. 2007, ApJ, 670, L131
López-Corredoira, M., & Sylos Labini, F. 2019, A&A, 621, A48
Lynds, B. T. 1962, ApJS, 7, 1
Machida, M. N., Matsumoto, T., Hanawa, T., & Tomisaka, K. 2006, ApJ, 645, 1227
MacLaren, I., Richardson, K. M., & Wolfendale, A. W. 1988, ApJ, 333, 821
Mac Low, M.-M., McKee, C. F., Klein, R. I., Stone, J. M., & Norman, M. L. 1994, ApJ, 433, 757
Magakian, T. Y. 2003, A&A, 399, 141
Matsumoto, T., Nakazato, T., & Tomisaka, K. 2006, ApJ, 637, L105
McCutcheon, W. H., Vrba, F. J., Dickman, R. L., & Clemens, D. P. 1986, ApJ, 309, 619
Medhi, B. J., Maheswar, G., Pandey, J. C., Kumar, T. S., & Sagar, R. 2008, MNRAS, 388, 105
Men'shchikov, A., André, P., Didelon, P., et al. 2010, A&A, 518, L103
Miniati, F., Jones, T. W., & Ryu, D. 1999, ApJ, 517, 242
Miville-Deschênes, M.-A., Martin, P. G., Abergel, A., et al. 2010, A&A, 518, L104
Moeckel, N., & Burkert, A. 2015, ApJ, 807, 67
Motte, F., Andre, P., & Neri, R. 1998, A&A, 336, 150
Mouschovias, T. 2001, ASP Conf. Ser., 248, 515
Myers, P. C. 1983, ApJ, 270, 105
Myers, P. C. 2009, ApJ, 700, 1609
Myers, P. C., Linke, R. A., & Benson, P. J. 1983, ApJ, 264, 517
Nakajima, Y., & Hanawa, T. 1996, ApJ, 467, 321
Neha, S., Maheswar, G., Soam, A., Lee, C. W., & Tej, A. 2016, A&A, 588, A45
Odenwald, S. F. 1988, ApJ, 325, 320
Odenwald, S. F., & Rickard, L. J. 1987, ApJ, 318, 702
Onishi, T., Mizuno, A., Kawamura, A., Tachihara, K., & Fukui, Y. 2002, ApJ, 575, 950
Ortiz-León, G. N., Loinard, L., Dzib, S. A., et al. 2018, ApJ, 869, L33
Ostriker, J. 1964, ApJ, 140, 1056
Padoan, P., & Nordlund, Å. 2002, ApJ, 576, 870
Palmeirim, P., André, P., Kirk, J., et al. 2013, A&A, 550, A38
Peretto, N., André, P., Könyves, V., et al. 2012, A&A, 541, A63
Pereyra, A., & Magalhães, A. M. 2004, ApJ, 603, 584
Pineda, J. L., Goldsmith, P. F., Chapman, N., et al. 2010, ApJ, 721, 686
Planck Collaboration Int. XXI. 2015, A&A, 576, A106
Planck Collaboration Int. XXXII. 2016, A&A, 586, A135
Planck Collaboration Int. XXXV 2016, A&A, 586, A138
Podio, L., Codella, C., Gueth, F., et al. 2016, A&A, 593, L4
Poglitsch, A., Waelkens, C., Geis, N., et al. 2010, A&A, 518, L2
Poleski, R. 2013, ArXiv e-prints [arXiv:1306.2945]
Polychroni, D., Schisano, E., Elia, D., et al. 2013, ApJ, 777, L33
Purcell, E. M. 1979, ApJ, 231, 404
Rautela, B. S., Joshi, G. C., & Pandey, J. C. 2004, Bull. Astron. Soc. India, 32, 159
Rivera-Ingraham, A., Ristorcelli, I., Juvela, M., et al. 2016, A&A, 591, A90
Rizzo, J. R., Morras, R., & Arnal, E. M. 1998, MNRAS, 300, 497
Rowell, N., & Kilic, M. 2019, MNRAS, 484, 3544
Sato, F., Mizuno, A., Nagahama, T., et al. 1994, ApJ, 435, 279
Scarrott, S. M., Rolph, C. D., & Tadhunter, C. N. 1991, MNRAS, 249, 131
Schmidt, G. D., Elston, R., & Lupie, O. L. 1992, AJ, 104, 1563
Schnee, S., Enoch, M., Noriega-Crespo, A., et al. 2010, ApJ, 708, 127
Schneider, N., Csengeri, T., Hennemann, M., et al. 2012, A&A, 540, L11
Schönrich, R., Binney, J., & Dehnen, W. 2010, MNRAS, 403, 1829
Shu, F. H., Adams, F. C., & Lizano, S. 1987, ARA&A, 25, 23
Smith, R. J., Glover, S. C. O., Klessen, R. S., & Fuller, G. A. 2016, MNRAS, 455, 3640
Soam, A., Maheswar, G., Bhatt, H. C., Lee, C. W., & Ramaprakash, A. N. 2013, MNRAS, 432, 1502
Soam, A., Maheswar, G., Lee, C. W., et al. 2015, A&A, 573, A34
Soam, A., Lee, C. W., Maheswar, G., et al. 2017, MNRAS, 464, 2403
Soler, J. D., Hennebelle, P., Martin, P. G., et al. 2013, ApJ, 774, 128
Soler, J. D., Alves, F., Boulanger, F., et al. 2016, A&A, 596, A93
Spezzano, S., Bizzocchi, L., Caselli, P., Harju, J., & Brünken, S. 2016, A&A, 592, L11
Stephens, I. W., Looney, L. W., Kwon, W., et al. 2013, ApJ, 769, L15
Stephens, I. W., Dunham, M. M., Myers, P. C., et al. 2017, ApJ, 846, 16
Straizys, V., Cernis, K., Kazlauskas, A., & Meistas, E. 1992, Balt. Astron., 1, 149
Suzuki, T., Ohishi, M., & Hirota, T. 2014, ApJ, 788, 108
Tafalla, M., & Hacar, A. 2015, A&A, 574, A104
Tafalla, M., Mardones, D., Myers, P. C., et al. 1998, ApJ, 504, 900
Tafalla, M., Myers, P. C., Caselli, P., Walmsley, C. M., & Comito, C. 2002, ApJ, 569, 815
Tafalla, M., Myers, P. C., Caselli, P., & Walmsley, C. M. 2004, A&A, 416, 191
Tomisaka, K. 1998, ApJ, 502, L163
Trick, W. H., Coronado, J., & Rix, H.-W. 2019, MNRAS, 484, 3291
Umekawa, M., Matsumoto, R., Miyaji, S., & Yoshida, T. 1999, PASJ, 51, 625
Umemoto, T., Iwata, T., Fukui, Y., et al. 1992, ApJ, 392, L83
Van Loo, S., Keto, E., & Zhang, Q. 2014, ApJ, 789, 37
Vázquez-Semadeni, E., Ballesteros-Paredes, J., & Klessen, R. S. 2003, ApJ, 585, L131
Vrba, F. J., Strom, S. E., & Strom, K. M. 1976, AJ, 81, 958
Walsh, A. J., Myers, P. C., & Burton, M. G. 2004, ApJ, 614, 194
Wang, J.-W., Lai, S.-P., Eswaraiah, C., et al. 2017, ApJ, 849, 157
Williams, J. P., de Geus, E. J., & Blitz, L. 1994, ApJ, 428, 693
Yonekura, Y., Dobashi, K., Mizuno, A., Ogawa, H., & Fukui, Y. 1997, ApJS, 110, 21
Yuan, J.-H., Wu, Y., Li, J. Z., Yu, W., & Miller, M. 2013, MNRAS, 429, 954
Zucker, C., & Chen, H. H.-H. 2018, ApJ, 864, 152